ABSTRACT

Title of dissertation: ELECTRON ACCELERATION DURING MACROSCALE NON-RELATIVISTIC MAGNETIC RECONNECTION

Harry Arnold
Doctor of Philosophy, 2021

Dissertation directed by: Professor James F. Drake
Department of Physics

In this thesis we developed the new model *kglobal* for the purpose of studying nonthermal electron acceleration in macroscale magnetic reconnection. Unlike PIC codes we can simulate macroscale domains, and unlike MHD codes we can simulate particles that feedback onto the fluids so that the total energy of the system is conserved. This has never been done before. We have benchmarked the model by simulating Alfvén waves with electron pressure anisotropy, the growth of the firehose instability, and the growth of electron acoustic waves. We then studied the results of magnetic reconnection and found clear power-law tails that can extend for more than two decades in energy with a power-law index that decreases with the strength of the guide field. Reconnection in systems with guide fields approaching unity produce practically no nonthermal electrons. For weak guide fields the model is extremely efficient in producing nonthermal electrons. The nonthermals contain up to $\sim 80\%$ of the electron energy in our lowest guide field simulation. These results are generally consistent with flare observations and specifically the measurements

of the September 10, 2017, flare.

Electron Acceleration during Macroscale Non-Relativistic Magnetic Reconnection

by

Harry Arnold

Dissertation submitted to the Faculty of the Graduate School of the
University of Maryland, College Park in partial fulfillment
of the requirements for the degree of
Doctor of Philosophy
2021

Advisory Committee:
Professor James Drake, Chair/Advisor
Professor Marc Swisdak
Professor Adil Hassam
Professor William Dorland
Professor M. Coleman Miller (Dean's Representative)

Acknowledgments

I would like to acknowledge my advisor, Professor James Drake, for taking me on as a graduate student and guiding me through graduate school. In addition to his skills as a teacher, it has been apparent that he has aided my career at every step of the way. I would also like to thank my co-advisor, Dr. Marc Swisdak. He was always available for any help that I might need, from coding advice to helping me navigate the administration to reminding me of various physical principles. My graduate experience was doubtlessly improved by these two experienced physicists. Thanks go also to Adil Hassam, Bill Dorland, and Cole Miller for graciously agreeing to sit on my committee.

I would also like to acknowledge my colleagues in the University of Maryland Plasma theory group: Elizabeth Paul, Mike Martin, Jimmy Juno, Matt Landreman, Rahul Gaur, Qile Zhang, Garreth Roberg-Clark, Rogerio Jorge, and Alessandro Geraldini. These friends provided excellent comradeship while we mutually explored the depths of plasma theory. Garreth Roberg-Clark deserves a special mention as we discussed both our research and lives in general extensively and provided moral support throughout our respective graduate school careers.

I would like to thank all my colleagues who aided my classroom studies in graduate school: Phillip Alvarez, Elizabeth Friedman, Julia Sell, Brittany Richman, and Linus Feder. Countless hours were spent pouring over textbooks in the pursuit of understanding everything from quantum physics to plasma physics.

Thanks are also due to my family, especially my parents, Ruth and Ken Arnold, for providing me with endless moral support, especially when I made the unusual

decision to obtain a second undergraduate degree. Finally I would like to thank my wife, Sylvia Arnold, who undoubtedly made the graduate experience far more enjoyable and significantly much less stressful. I have no idea how I would have done it without her.

Table of Contents

List of Figures

Chapter 1: Introduction

1.1 Magnetic Reconnection

Although the world we live in is primarily made up of liquids, solids, and gases, there is a fourth state of matter called plasmas. In fact, observations of the universe suggest that 99.999% of all observable matter is plasma [1]. This makes studying plasma extremely important for understanding the universe that we live in. While the physics of plasmas covers a large amount of material, in this thesis we concern ourselves with a process called magnetic reconnection. During magnetic reconnection magnetic fields that are initially pointing in opposite directions can "reconnect" as illustrated in Fig. 1.1. The field lines flow towards the so called "X-line" where the in-plane magnetic field vanishes in a current layer between the two regions of oppositely pointing magnetic fields. After reconnection the new field lines are highly bent, as can be seen in Fig. 1.1 on the right and left sides, and move outwards at a characteristic speed called the Alfvén speed. As the field lines move their magnetic tension pushes the plasma analogous to a stretched rubber band snapping forward. This process then heats the plasma and can accelerate particles to extremely high energies.

Magnetic reconnection plays an important role in many different phenomena

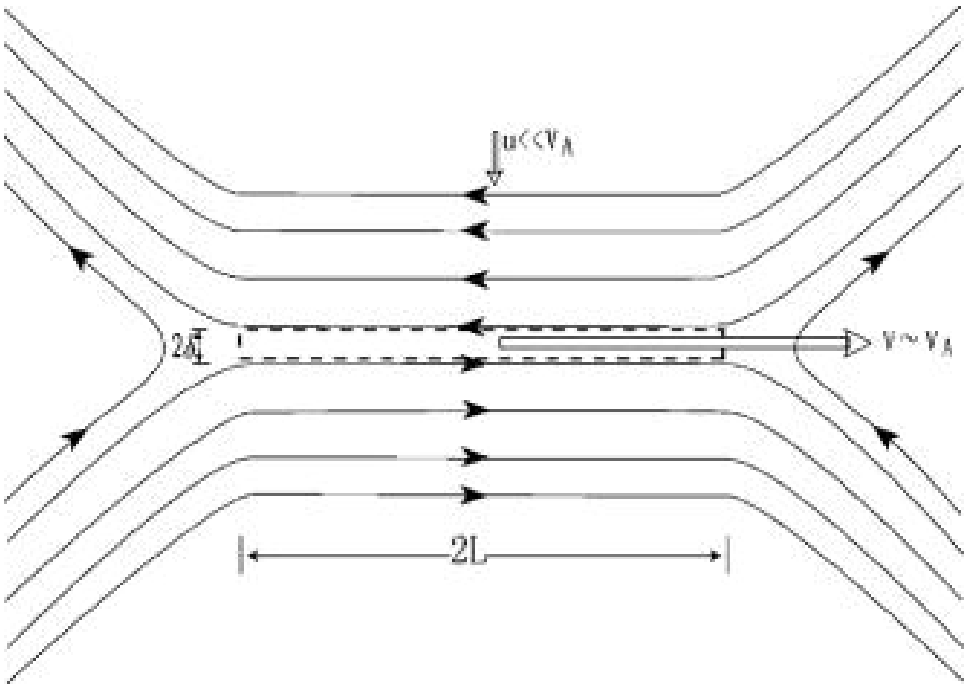

Figure 1.1: A schematic of magnetic reconnection. Initially oppositely directed magnetic field lines reconnect and form bent field lines. Reprinted from [2]

that affect life on Earth. It is responsible for the sawtooth crash seen in tokamaks that dissipates magnetic energy and disrupts magnetic confinement of high temperature plasma. This is a strong obstacle that needs to be overcome to make fusion economically feasible. Reconnection is also responsible for solar flares and coronal mass ejections. These events typically release 10^{27} ergs/sec or about 10 million nuclear bombs exploding every second. While this process occurs on the Sun, human society can be affected if Earth is hit by the radiation associated with this event. While that energy diffuses as it travels outward from the sun, a direct hit on Earth can still disrupt everyday life: On March 10, 1989 the effects of a flare were powerful enough to knock out Quebec's electrical grid and trigger northern lights that could be seen as far south as Cuba. Additionally, the radiation from solar flares can threaten the lives of astronauts, especially if humans attempt interplanetary travel. In this thesis we focus on the development of a new computational model that can be used to explore electron acceleration during magnetic reconnection in macroscale systems and apply it to understand particle acceleration in solar flares.

1.2 Observations of Macroscale Reconnection

Observations of solar flares suggest that a large fraction of the energy released appears as energetic electrons and ions [3–5]. Solar observations also indicate the highest energy electrons are closest to the inferred position of the x-line [6]. In recent observations of over-the-limb flares the limb of the sun blocked the intense emission from the chromosphere, which enabled direct measurement of the high

corona where magnetic energy was released in the flare [7,8]. The surprise was that a large fraction of the electrons in the high emission region were in the energetic component, indicating that most electrons in the region underwent acceleration. Such observations are consistent with the large number of accelerated electrons seen in flares. Further, the total pressure of these energetic particles was comparable to that of the magnetic field. That energetic electrons can be efficiently produced during reconnection is not limited to flares. During *in situ* satellite measurements in the distant magnetotail energetic electrons in excess of 300 keV were produced. They were broadly peaked around the reconnection x-line rather than localized in boundary layers, suggesting that electrons were able to wander over a broad region [9].

The observations pose significant challenges to models of electron and ion acceleration during magnetic reconnection. These challenges include: large numbers of electrons undergoing strong heating in flares with the pressure of the energetic component approaching that of the reconnecting magnetic field; the energetic electrons peaking in a broad region around the x-line and not in localized boundary layers; and the particle spectra exhibiting a power-law form at high energy.

These observations rule out the classical picture in which reconnection-driven particle acceleration takes place in a boundary layer associated with a single, large-scale reconnection site. Such a single x-line model can not explain the large number of energetic particles produced during reconnection nor their broad spatial distribution. Further, reconnected magnetic field lines release most of their energy as they expand downstream of the x-line rather than in the diffusion regions around the

x-line where the topological change in magnetic structure takes place.

On the other hand, it is also now established that current layers typically spawn multiple magnetic islands, bubble like objects encircled by a magnetic field line, in 2D systems [10, 11] or become turbulent due to the generation of multiple x-lines with variable tilt angles in 3D systems [12–16], especially in the presence of strong magnetic fields in the out-of-plane direction, or guide field, in Fig. 1.1. Observations of flux transfer events (FTEs) at the magnetopause [17], flux ropes in the magnetotail [18,19] and downflowing blobs during reconnection in the corona [20, 21] support the multi-island, multi-x-line picture of reconnection. That reconnection becomes turbulent is also consistent with recent solar flare observations in which the production of energetic electrons was correlated with the onset of turbulent flows [22].

1.3 Electron energy gain

Observations suggest that reconnection-driven particle acceleration takes place in a multi-island or turbulent reconnecting environment rather than in a single, large-scale reconnection site. To understand particle acceleration in such an environment, recall that as particles travel along a magnetic field line they also orbit the field centered on a point called the guiding center. Thus we can average over the gyration and write the basic equation for the rate of energy gain of particles in a guiding center system after summing over all particles in a local region [23].

$$\frac{dW}{dt} = E_{||}J_{||} + \frac{P_{\perp}}{B}\left(\frac{\partial B}{\partial t} + \mathbf{v}_E \cdot \nabla B\right) + (P_{||} + np_{||}v_{||})\mathbf{v}_E \cdot \boldsymbol{\kappa} \tag{1.1}$$

where W is the total kinetic energy density, $\mathbf{v}_E = c\mathbf{E} \times \mathbf{B}/B^2$, $v_{||}$ and $p_{||}$ are the bulk parallel velocity and momentum, and the curvature of the magnetic field is $\boldsymbol{\kappa} = \mathbf{b}\cdot\nabla\mathbf{b}$ with $\mathbf{b}$ the unit vector along $\mathbf{B}$. The parallel and perpendicular pressures are $P_{||}$ and $P_{\perp}$ and n is the density. The equations apply to any species for which the guiding-center approximation is valid. However, for ions an additional term, the dot product of the polarization drift into the electric field, is required since the kinetic energy associated with the $\mathbf{E}\times\mathbf{B}$ drift is not negligible. The first term in Eqn. (1.1) is the acceleration by the parallel electric field. The second term corresponds to perpendicular heating or cooling due to the conservation of the magnetic moment μ (Betatron acceleration). The third term drives parallel acceleration and arises from the first-order Fermi mechanism [24–26]. Freshly reconnected field lines downstream from a reconnecting x-line accelerate as a result of the tension force that causes them to "straighten". Particles that reflect from this moving field line receive a Fermi "kick" and thereby gain energy. This is illustrated in Fig. 1.2. The bent field line moves outwards at the Alfvén speed, C_A, and the particle streams towards the bent filed line at a speed v_0. But in the frame of the magnetic field line the particle moves at a speed $v_0 + C_A$ and reflects off the field line just as a ball bounces off a wall, thus the particle leaves moving at the same speed. When you go back to the "laboratory" frame where the field line is moving at the Alfvén speed the particle is moving at $v_0 + 2C_A$ and has gained energy.

Betatron acceleration is typically not important during reconnection since the release of magnetic energy leads to a reduction of B and therefore the perpendicular temperature [27]. Depending on the strength of the ambient guide field either $E_{||}$ or

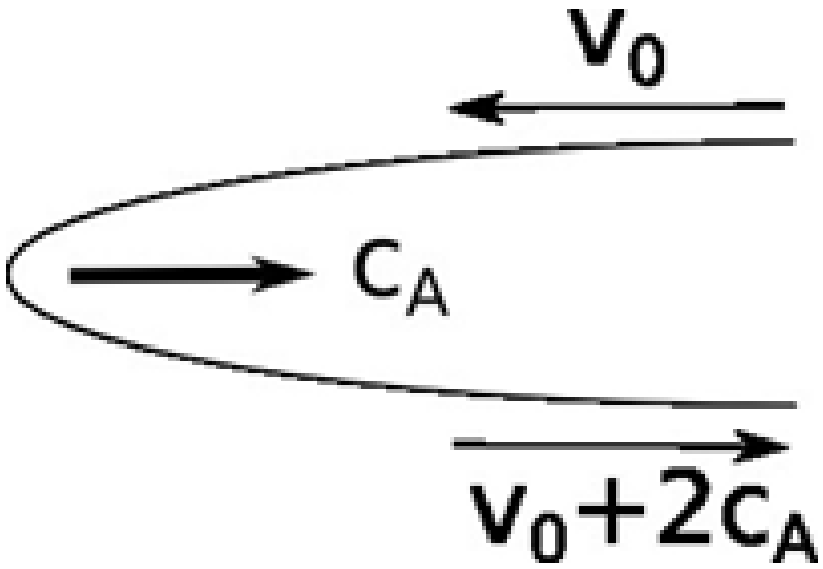

Figure 1.2: A bent field line moving at the Alfvén speed, C_A, with an incoming particle with an initial speed v_0. After receiving a Fermi kick and gaining energy the particle leaves at the speed $v_0 + 2C_A$.

Fermi reflection dominates electron heating during reconnection. Fermi reflection dominates for weak to modest guide fields while $E_{||}$ dominates for large guide fields [27]. A recent important discovery is that energetic electron production plunges in the strong guide field limit where $E_{||}$ dominates and therefore $E_{||}$ is an inefficient driver of energetic particles [16, 28]. This result also suggests that high frequency waves, such as double layers and electron solitary waves, which have been identified in both observations and simulations of reconnection [29], are not a major driver of energetic electrons during reconnection. Importantly, in a regime where Fermi reflection dominates, particle energy gain and magnetic energy release are directly linked (consistent with flare observations) [10, 30], energetic particles spread over broad regions and are not localized in narrow boundary layers [15, 16], and large numbers of particles undergo acceleration.

However, it is known that a large-scale parallel electric field (not localized in boundary layers) facilitates electron energy gain by confining electrons within the reconnection exhaust such that they undergo multiple Fermi kicks [31–34]. Thus, it is of interest to include this large scale parallel electric field in our model to properly model the energy gain of low energy electrons. This potential is not, however, important to the dynamics of very energetic electrons. This field arises from parallel gradients in the electron pressure and points away from the current sheet in the reconnection exhaust. In an open system it drives a return current of cold electrons that balances the current associated with escaping hot electrons to maintain zero net parallel current.

1.4 Limitations of Common Plasma Models

There are several existing models for plasma simulations. Each model has advantages and disadvantages and no model can perfectly simulate a plasma. The reason for this inherent limitation is because in order to perfectly simulate a plasma the positions and velocities of every particle needs to be known at every time. Further every particle will generate electric and magnetic fields that then effect every other particle. To simulate this system would be very computationally expensive and is impractical since the time required to perform a simulation scales like the number of particles squared, N^2. Thus, broadly speaking, various simplifications have led to two sorts of models.

The first is called a particle-in-cell (PIC) model. This model treats the plasma as "macro-particles". Each macro-particle represents a density of particles and has a position and velocity. The electric and magnetic fields are then determined at regular intervals on a grid due to the positions and motion of all the macro-particles in the corresponding grid cell. Then the fields accelerate the particles through the Lorentz force. This drastically reduces the number of computations during the simulation, resulting in the required time scaling like $Nlog(N)$. This model is excellent when studying kinetic-scale effects since a PIC model needs to resolve the smallest physical scales. The second kind of model is called a magnetohydrodynamic model (MHD). This model treats the plasma as a fluid by taking moments of the Vlasov equation. In this model small scales are averaged out and individual particles do not exist. Thus, studying large scale systems, such as the Earth's magnetosphere, are possible

in this model. The motion and energization of particles can be studied in these models through a "test particle" approach. However, the test particles do not feed back onto the MHD fluid and fields and therefore the total system, including the test particles, does not conserve energy.

Energetic particle spectra in heliospheric observations typically take the form of high energy power-law tails. On the other hand, the particle spectra in PIC simulations of reconnection in the non-relativistic regime (Alfvén speed much smaller than the velocity of light) typically do not form power-laws [16,27] except in the limit in which the upstream plasma pressure is much lower than that of the magnetic field (extremely low plasma β) [35]. Simple "particle-in-a-box" models in which energy drive and loss mechanisms are included exhibit power-law spectra [30, 36]. The hardest spectra from such models have distribution functions f that scale as v^{-5}, which correspond to the upper limit so that the integrated particle energy remains finite. The particle fluxes at this limit scale as $\varepsilon^{-1.5}$ with ε the particle energy. Electron fluxes that scale as $\varepsilon^{-1.5}$ have been observed in solar flares [37]. Ion fluxes typically scale as $\varepsilon^{-1.5}$ in the solar wind [38] and in the outer heliosphere [39, 40]. Thus, simulations of reconnection-driven particle acceleration that are large enough to include realistic loss mechanisms appear to be required to explain observations.

The fundamental question is how to explore particle acceleration in macro-scale reconnecting systems such as the solar corona where the separation between kinetic scales and macro-scales approaches 10^{10} (the Debye length is less than a centimeter for $n \sim 10^{10}/\mathrm{cm}^3$ and $T_e \sim 100\mathrm{eV}$ while macro-scales approach $10^4\mathrm{km}$). The development of Parker-like transport equations that describe reconnection-driven

particle acceleration illuminate the important physical processes that control spectra (pressure anisotropy, feedback on the Fermi drive, particle loss versus energy gain times) [30, 41–43]. They also yield guidelines on the range of spectral indices that are possible in reconnecting systems. However, such models are not able to directly describe the reconnection dynamics of a given event such as an impulsive flare in the sun's atmosphere even when they are paired with the MHD description of the system – scattering in such models is assumed to be strong enough so that the energetic particles are tied to the local fluid and so are unable to stream along ambient magnetic field lines [43]. Such strong scattering, however, is inconsistent with solar flare observations [44].

Exploring the dynamics of test particles in the MHD fields produces useful information about how particles gain energy [45–48]. However, the energy going into the energetic particles can run away since there is no feedback on the MHD fields. It is also possible to embed PIC models into large-scale MHD descriptions at selected locations where reconnection takes place [49]. However, such models presume that particle energy gain is highly localized in space around isolated x-lines, which is not consistent with the description of particle energy gain during the development and interaction of macro-scale magnetic islands or the development of turbulence in large-scale current layers.

The problem with conventional PIC codes in the context of modeling large-scale systems is that the Debye length has to be resolved to avoid non-physical heating of the electron macro-particles. Implicit PIC models avoid this constraint but still need to resolve the electron and ion inertial scales [50]. Conventional hybrid

codes (fluid electrons and macro-particle ions) can not model electron acceleration and must still resolve the ion inertial scale and the ion Larmor radius and therefore can not be used to explore energetic particle spectra in macroscale systems.

The fundamental question is whether kinetic scale boundary layers play an essential role in the development of particle energy gain during impulsive flares in macro-scale systems such as the sun's corona. The rate of reconnection in kinetic descriptions corresponds to inflows that are around $0.1C_A$ where C_A is the Alfvén speed based on the upstream reconnecting magnetic field [51–53]. On the other hand, MHD descriptions of reconnection at low resistivity generate multiple magnetic islands and yield reconnection rates that, while somewhat slower than in kinetic models, are, nevertheless, insensitive to plasma resistivity [54–56]. The inclusion of current-driven resistivity can boost MHD reconnection rates to values comparable to kinetic models. Kinetic boundary layers control the regions where $E_{||}$ is non-zero [57,58]. However, it is Fermi reflection and not $E_{||}$ that is the dominant driver of energetic particles. Particle energy gain from Fermi reflection takes place over macro-scale regions where magnetic fields are releasing energy and takes place even where $E_{||} = 0$. Physically, particles moving along bent field lines have curvature drifts along the reconnection electric field and therefore gain energy as long as $\boldsymbol{\kappa} \cdot \mathbf{v}_E$ is positive. The conclusion therefore is that including kinetic-scale boundary layers is not required to describe the dynamics of energy gain of the most energetic particles in macroscale systems. The MHD model is a reasonable description of heating during magnetic reconnection – either through the formation of switch-off slow shocks in anti-parallel reconnection or a combination of rotational discontinuities

and slow shocks in the case of reconnection with a guide field [59].

We conclude therefore that we can explore particle acceleration during magnetic reconnection in macroscale systems without resolving the kinetic scale boundary layers that limit traditional kinetic models. Here we present a novel computational model that combines the MHD description of the plasma dynamics with a macro-particle description but in which all kinetic scales are ordered out of the system of equations. The macro-particles can be small in number density but can contribute a pressure that can be comparable to the pressure of the reconnecting magnetic field. They move within the MHD grid and are advanced in parallel with the fluid equations using the guiding center equations based on the MHD electric and magnetic fields. The particles feed back on the MHD fluid through their gyrotropic pressure tensor. The entire system conserves the total energy, including that of the MHD fluid (ions and the bulk electrons), the magnetic field and the kinetic energy of the macro-particles. In the early phase of exploration of this model, we are treating only electrons as macroparticles but the ions can also be similarly treated.

There have been earlier efforts to couple the MHD equations to a gyro-kinetic model for studying the stability of Alfvén waves [60] and the internal kink mode in tokamaks [61]. However, the gyrokinetic model orders out Fermi reflection, which for exploring particle acceleration during reconnection is essential. The basic ordering that we adopt is consistent with that discussed by Kulsrud in which Fermi reflection is retained [62]. Overall energy conservation was not discussed in this previous work. Others have coupled the MHD equations to a general kinetic particle description [63].

The importance and challenge of producing a set of equations that conserves energy exactly has been discussed previously [64].

The *kglobal* simulations produce power-law spectra of energetic electrons that extend nearly three decades in energy and at the same time produce the super-hot thermal electrons that characterize flare observations [7, 8, 65]. Consistent with observations, the total energy content of the nonthermal electrons can exceed that of the hot thermal electrons even though the number density of the nonthermals is less than the hot thermals. The simulations have been carried out with a variety of values of the initial ambient out-of-plane guide field and reveal that the strength of the guide field strongly impacts the energy content of the nonthermal electrons and their power-law index. Specifically, a guide field that exceeds the reconnecting magnetic field suppresses nonthermal electron acceleration by increasing the effective radius of curvature of reconnecting magnetic field lines and therefore suppresses the dominant Fermi drive mechanism and the production of nonthermal electrons. In contrast, the size of the global system has relatively little influence on the production of nonthermal electrons.

1.5 Outline of Thesis

In Chap. 2, we describe the *kglobal* model in detail and present tests of the model that verify its capabilities. The model consists of an MHD backbone with macroparticle electrons distributed on the MHD grid. The guiding center equations with the MHD electric and magnetic fields describe the motion and energy gain

of the macroparticle electrons. These electrons feedback onto the MHD fluids and fields and conserve energy. We show that *kglobal* correctly simulates Alfvén waves in the presence of a pressure anisotropy, which is crucial for modeling Fermi reflection since pressure anisotropy can reduce magnetic field tension and the associated Fermi drive mechanism. Specifically, we demonstrate that the model reproduces the correct growth rate of the linear firehose instability, which onsets when the local field-line tension goes to zero.

In Chap. 3, we describe the addition of a large scale parallel electric field in the *kglobal* model. This stems from parallel gradients in the electron pressure tensor and points away from the current sheet in the reconnection exhaust. It is believed that this electric field is capable of reflecting low energy electrons back into the reconnection exhaust to receive multiple Fermi kicks and gain energy. This parallel electric field also develops to drive a return current to maintain zero current when energetic electrons escape along open field lines. We then benchmark *kglobal* against a PIC model and correctly match the Landau damping rate of the electron acoustic mode, which onsets as energetic electrons stream outward on open field lines.

In Chap. 4, we present results from 2D magnetic reconnection using the new *kglobal* model. Reconnection begins from particle noise and produces multiple islands (or flux ropes since they consist of an axial magnetic field wrapped by the inplane magnetic field) that merge, forming larger islands and accelerating electrons. The pressure anisotropy from the electron macroparticles becomes large enough to eliminate the magnetic tension force along outflow exhausts and within islands when electron acceleration is strong. Clear power-law tails extending nearly 3 decades

in energy develop for weak guide fields. Importantly, the power-law index depends strongly on the guide field such that for low guide fields a hard spectrum is observed. An analytic model is presented that reproduces the spectral indices obtained in the simulations and reveals the strong dependence on the guide field. Unsurprisingly, for low guide fields, i.e. harder spectra, more energy is concentrated in the nonthermal electrons. Finally we compare our results with observations of solar flares.

In Chap. 5 we present conclusions, discuss the results in the context of previous efforts to explore reconnection-driven electron acceleration, and suggest future extensions of this work.

Chapter 2: A computational model for exploring particle acceleration during reconnection in macroscale systems

In this chapter we describe the *kglobal* model. Testing shows that the model correctly describes the propagation of an Alfvén wave in the presence of an electron pressure anisotropy and the linear firehose instability. These are two important benchmarks since the bent, reconnected magnetic field lines travel at the Alfvén speed and reconnection is throttled by the suppression of field-line tension as a plasma approaches firehose marginal stability. We include a fourth order hyperviscosity term to prevent grid scale instabilities and to cutoff the firehose instability at high k. The material in this chapter has been adapted from [23] with permission from the authors.

2.1 Basic Equations and Conservation Properties

We treat a system with three distinct classes of particles: ions of density n and temperature T_i, cold electrons with density n_c and temperature T_c and energetic electrons with density $n_h = n - n_c$. The hot electrons will be treated as macroparticles that are evolved through the MHD grid by the guiding center equations.

Momentum equations can be written down for each of the three species, the ions

$$m_i n \frac{d\mathbf{v_i}}{dt} = ne\mathbf{E} + \frac{ne}{c}\mathbf{v}_i \times \mathbf{B} - \nabla P_i, \tag{2.1}$$

the cold electrons

$$m_e n_{ec} \frac{d\mathbf{v_{ec}}}{dt} = -n_{ec} e\mathbf{E} - \frac{n_{ec} e}{c}\mathbf{v}_{ec} \times \mathbf{B} - \nabla P_{ec}, \tag{2.2}$$

and the hot electrons

$$\frac{\partial(n_{eh}\bar{\mathbf{p}}_{eh})}{\partial t} = -n_{eh} e\mathbf{E} - \frac{n_{eh} e}{c}\bar{\mathbf{v}}_{eh} \times \mathbf{B} - \nabla \cdot \mathbb{T}_{eh}. \tag{2.3}$$

$\mathbf{v}_i$, $\mathbf{v}_{ec}$ and $\bar{\mathbf{v}}_{eh}$ are the ion and electron cold and hot velocities and $\bar{\mathbf{p}}_{eh}$ is the average hot electron momentum (an average of the local momenta of individual particles). The hot electron stress tensor $\mathbb{T}_{eh}$ includes both the pressure and convective derivatives and as a consequence the inertia term in Eq. (2.3) does not include the convective derivative. The hot electron stress tensor is given by

$$\mathbb{T}_{eh} = \int d\mathbf{p}_e \frac{\mathbf{p}_e \mathbf{p}_e}{m_e \gamma_e} f \tag{2.4}$$

with $\mathbf{p}_e$ the hot electron momentum with distribution f and γ_e is the relativistic Lorentz factor. The form of $\mathbb{T}_{eh}$ for guiding center particles and the reason for writing the hot electron momentum equation in this form will be clarified later. These equations are formally exact if there are mechanisms for maintaining the isotropy of P_i and P_{ec}. The usual challenge in deriving the MHD equations from the multi-fluid equations is that the electric field and Lorentz force terms are formally larger than the other terms in the equations. In Eq. (2.1), for example, taking $v_i \sim V_A$ and $d/dt \sim V_A/L$, the inertia term is of order $d_i/L \ll 1$ and therefore small

if the ion inertial length $d_i = V_A/\Omega_i$ is much smaller than the system scale length L. The usual procedure is then to sum the two fluid equations or in the present case the three fluid equations, which eliminates the electric field completely and reduces the Lorentz forces to the $\mathbf{J} \times \mathbf{B}/c$ force of the usual MHD equation. Since $J \sim cB/4\pi L \sim neV_A(d_i/L) \ll neV_A$, the inertial and $\mathbf{J} \times \mathbf{B}$ terms in the MHD equations are the same order.

In the present system we carry out the same procedure while discarding the electron inertial terms, which are small as long as $L \gg d_e$ with d_e the electron inertial length. We emphasize that we are discarding only the inertia of the bulk flow associated with the hot electrons and not the inertia associated with individual hot electrons. The dominant motion of individual hot electrons in the guiding center limit is parallel to the ambient magnetic field. The perpendicular motion arises from $\mathbf{v}_E$ with the various perpendicular gradient drifts being much smaller. The large parallel velocities of the hot electrons largely cancel when summed to produce a large parallel pressure but not a large streaming velocity. Because we are discarding the electron fluid inertia, in summing the three momentum equations we also discard the parallel electric field and the parallel pressure gradient of the hot electrons. The hot electrons are unable to couple to the MHD fluid along the ambient magnetic field through their parallel pressure gradient. Their parallel motion is instead controlled by the inertia of individual particles and electromagnetic forces. They act only on the MHD fluid through their forces perpendicular to $\mathbf{B}$. An extension of such a model to include a finite macroscale parallel electric field is discussed at the end of

the chapter. Thus, summing the three momentum equations yields

$$\rho \frac{d\mathbf{v}}{dt} = \frac{1}{c}\mathbf{J} \times \mathbf{B} - \nabla P - (\nabla \cdot \mathbb{T}_{eh})_{\perp}\,, \tag{2.5}$$

where we have suppressed the subscript so that $\mathbf{v}$ is the fluid velocity with mass density ρ and $P = P_i + P_{ec}$. The energetic particles act on the MHD fluid through their stress tensor. It is convenient, however, to express this force in terms of the hot electron current $J_{ehT\perp}$ driven by the stress tensor. This current is obtained from the hot electron momentum equation by first subtracting the dominant current associated with $\mathbf{v}_E$ (which cancels that of the ions and cold electrons) from $\mathbf{J}_{eh}$. This yields

$$\mathbf{J}_{ehT\perp} = \frac{c}{B}\mathbf{b} \times \nabla \cdot \mathbb{T}_{eh} \tag{2.6}$$

We now proceed to simplify the form of $\mathbb{T}_{eh}$ for guiding center electrons. The stress tensor can be written in two distinct components associated with the averaged hot electron convection and the pressure. In the direction perpendicular to $\mathbf{B}$, the dominant perpendicular motion of the hot electrons is given by $\mathbf{v}_E$ with other drifts being smaller in the ratio of the Larmor radius to the macroscale L. For $v_E \sim V_A$ the inertia associated with this perpendicular motion is negligible as long as $m_e/m_i \ll \beta_{eh\perp} \sim 1$. In this limit the stress tensor takes the usual gyrotropic form

$$\mathbb{T}_{eh} = T_{eh||}\mathbf{bb} + P_{eh\perp}(\mathbb{I} - \mathbf{bb}), \tag{2.7}$$

where $\mathbb{I}$ is the unit tensor, $T_{eh||}$ is the stress tensor along the magnetic field $\mathbf{B}$ and $P_{eh\perp}$ is the usual perpendicular pressure,

$$P_{eh\perp} = \int d\mathbf{p}_e \frac{p_{e\perp}^2}{2m_e\gamma_e} f, \tag{2.8}$$

where in the frame drifting with $\mathbf{v}_E$, $f = f(\mathbf{x}, p_{e||}, p_{e\perp}, t)$ since there is no other mean drift perpendicular to $\mathbf{B}$. $T_{eh||}$ includes the mean parallel drifts of the hot electrons and can be written as a combination of the usual parallel pressure $P_{eh||}$ plus the mean parallel convection terms,

$$T_{eh||} = \int d\mathbf{p}_e \frac{p_{e||}^2}{m_e \gamma_e} f = P_{eh||} + n_{eh} \bar{p}_{eh||} \bar{v}_{eh||} \tag{2.9}$$

with

$$P_{eh||} = \int d\mathbf{p}_e (p_{e||} - \bar{p}_{eh||}) \left(\frac{p_{e||}}{m_e \gamma_e} - \bar{v}_{eh||} \right) f. \tag{2.10}$$

The hot electron parallel bulk streaming terms in Eq. (2.9) are nominally much smaller than the parallel pressure since

$$n_h \bar{p}_{eh||} \bar{v}_{eh||} \sim \frac{m_e J_{||}^2}{n e^2} \sim \frac{B^2}{4\pi} \frac{d_e^2}{L^2} \sim P_{eh||} \frac{d_e^2}{L^2} \ll P_{eh||}. \tag{2.11}$$

On the other hand, we demonstate below that exact energy conservation requires that this nominally small contribution to $T_{eh||}$ be retained since these contributions appear in the expression for electron energy gain given in Eq. (1.1). With the form of the stress tensor given in Eq. (2.7), the hot electron current can be expressed as [66]

$$\mathbf{J}_{ehT\perp} = \frac{c}{B} (T_{eh||} - P_{eh\perp}) \mathbf{b} \times \boldsymbol{\kappa} + \frac{c}{B} \mathbf{b} \times \nabla P_{eh\perp}. \tag{2.12}$$

An equivalent form for the hot electron current is

$$\mathbf{J}_{ehT\perp} = \frac{c}{B} \mathbf{b} \times \left(P_{eh\perp} \nabla \ln(B) + T_{eh||} \boldsymbol{\kappa} \right) - c \left(\nabla \times \frac{P_{eh\perp} \mathbf{b}}{B} \right)_\perp, \tag{2.13}$$

where the first term on the right is the gradient B drift, the second is the curvature drift and the third is the magnetization current [67]. The MHD equation with

energetic electron feedback can then be written as

$$\rho\frac{d\mathbf{v}}{dt} = \frac{1}{c}\mathbf{J}\times\mathbf{B} - \nabla P - \frac{1}{c}\mathbf{J}_{ehT\perp}\times\mathbf{B}. \tag{2.14}$$

The calculations leading to Ohm's law in this three species system parallel that of the electron-ion system. As discussed previously, the dominant terms in Eqs. (2.2)-(2.3) are the electric field and Lorentz terms. Adding the two electron equations and discarding the pressures and stress tensor, we obtain

$$\mathbf{E} = \frac{1}{nc}(n_{ec}\mathbf{v}_{ec} + n_{eh}\mathbf{v}_{eh})\times\mathbf{B} = \frac{1}{nec}\mathbf{J}\times\mathbf{B} - \frac{1}{c}\mathbf{v}\times\mathbf{B} \simeq -\frac{1}{c}\mathbf{v}\times\mathbf{B}, \tag{2.15}$$

where we have added and subtracted $n\mathbf{v}$ in the Lorentz force and again used the fact that $J \ll nev$ to eliminate the $\mathbf{J}\times\mathbf{B}$ or Hall term in Ohm's law. Thus, Ohm's law, which determines $\mathbf{E}$ in terms of $\mathbf{v}$ is unchanged from the usual MHD prescription. The equations for the pressure P and mass density ρ are also unchanged.

The model is completed by the guiding-center equations for the hot electrons [68]

$$\frac{d}{dt}p_{e||} = p_{e||}\mathbf{v}_E\cdot\boldsymbol{\kappa} - \frac{\mu_e}{\gamma_e}\mathbf{b}\cdot\nabla B \tag{2.16}$$

with $p_{e||}$ the parallel momentum of a macroparticle electron with its magnetic moment given by

$$\mu_e = p_{e\perp}^2/2B. \tag{2.17}$$

$p_{e\perp}$ is determined from the conservation of μ_e. The particle velocity is given by $\mathbf{v}_E$ and the parallel streaming $v_{eh||} = p_{eh||}/(\gamma_e m_e)$ along $\mathbf{B}$, the curvature and gradient B drifts being smaller in the ratio of the Larmor radius to the macroscale L. The ordering of the hot electron drifts and their energy gain in Eqs. (2.16)-(2.17) are

equivalent to Kulsrud's guiding center description [62]. A critical goal in developing a credible set of equations to describe particle acceleration is to establish energy conservation. By taking the dot product of Eq. (2.14) with $\mathbf{v}$ and integrating over space the energy conservation relation takes the form

$$\frac{d}{dt}W_{MHD} = -\int d\mathbf{x}\ \mathbf{J}_h \cdot \mathbf{E} = -\frac{d}{dt}W_h$$
$$= -\int d\mathbf{x}\left[T_{eh||}\mathbf{v}_E \cdot \boldsymbol{\kappa} + \frac{P_{eh\perp}}{B}\left(\frac{\partial B}{\partial t} + \mathbf{v}_E \cdot \nabla B\right)\right] \quad (2.18)$$

where W_{MHD} is the usual energy in the MHD description, including the kinetic energy of the bulk flow, the thermal energy and magnetic energy. dW_h/dt is the rate of change of the energy of the hot electrons. dW_h/dt in Eq. (2.18) is equal to the spatial integral of the rate of energy gain in Eq. (1.1). We again note that the convective terms in the curvature in Eq. (2.18) are nominally small since $d_e^2/L^2 \ll 1$ but must be retained so that the energy gain in Eq. (1.1), which follows from Eq. (2.16) and the conservation of μ_e, matches that in Eq. (2.18). Having equations that exactly conserve energy facilitates testing the model and is desirable [64].

The equations presented above provide a complete self-consistent system for exploring the production of energetic electrons in macroscale systems. Since the electrons are evolved in the fields from the MHD equations, the artificial heating associated with the PIC model when the Debye length is not resolved is not an issue. Similar equations can be written down that also include energetic ions although the neglect of their inertia requires that their number density be small. Beyond energy conservation, an important consideration is whether the equations properly describe the feedback of the energetic component on the MHD fluid. It is straightforward

to show that the inclusion of an ambient pressure anisotropy in the hot component through $\mathbb{T}_{eh}$ yields the correct firehose stability criterion. In the case of magnetic reconnection the firehose stability boundary plays an important role in throttling reconnection [25, 26] and in controlling the spectral index of the energetic particles resulting from reconnection [30]. The firehose stability boundary will act similarly in this model if the pressure in the energetic component is too high. With these equations the production of energetic particles in realistic macroscale systems can be explored where realistic losses can be included and the realistic spectra of synchrotron emission from the volume and Bremsstrahlung emission at system boundaries can be calculated for direct comparison with X-ray observations from satellite missions such as Ramaty High Energy Solar Spectroscopic Imager (RHESSI) and ground-based radio observatories such as the Nobeyama Radioheliograph (NoRH) [69] or the Extended Owens Valley Solar Array (EOVSA) [70].

2.2 Tests of the *kglobal* model

As discussed in the previous section, the pressure anisotropy of the energetic electrons plays an important role in throttling magnetic reconnection and limiting the energy gain of those particles [25, 26, 30]. Thus to ensure the model correctly describes the impact of pressure anisotropy on magnetic field dynamics we benchmark the code with two simple wave modes that are evolved in a system with an imposed initial pressure anisotropy: the linear propagation of stable, circularly polarized Alfvén waves; and the linear growth of firehose modes. The correct solutions

of both of these tests are, of course, well known [71].

The new computational model was constructed by merging the fluid evolution equations of the *f3d* code [72] (with the Hall terms in Ohm's law removed) and the particle treatment in the *p3d* code [73], modified to step the particles in the guiding center limit. Time stepping is with a second order trapezoidal leapfrog scheme with a fourth order viscosity added to each of the fluid equations to prevent the buildup of noise at the grid scale.

In this new model the magnetic field strength, B_0, and density, n_0, define the Alfvén speed, $V_A = \sqrt{B_0^2/4\pi m_i n_0}$. Since there are no kinetic scales that enter the equations, lengths and times are normalized to a macroscale length, L, and Alfvén crossing time, $\tau_A = L/V_A$. This normalization allows us to set the physical distance of the longest dimension in our simulations to $2\pi L$ where L can be any macroscopic scale length. Electric fields and temperatures are normalized to $V_A B_0/c$ and $m_i V_A^2$, respectively. A fourth order hyperviscosity, $\nu\nabla^4$, is included for every quantity evolved on the grid (magnetic field, ion density, momentum and pressure and cold electron pressure).

The tests were carried out in a system with two space dimensions with $B_x = B_0$. The ion to hot electron mass ratio is set to 25 (the cold electrons are massless). For a given hot electron pressure and density the mass ratio controls the streaming velocity of electrons through the system. For linear waves with an imposed initial pressure anisotropy the evolution of the pressure does not enter the equations so the value of electron mass does not influence the dynamics. The temperature of the ions and the cold electrons was 1/12. For the hot electrons, the temperature was varied

to control the magnitude of the anisotropy of their pressure tensor. The box size was varied from 256 x 64 cells to 512 x 256 cells and there were 160-320 particles per grid cell.

In the first benchmark of the model we propagated a circularly-polarized Alfvén wave along a magnetic field in a system with an imposed hot electron pressure anisotropy. We initialized the simulations with a perturbation with a wavelength equal to the size of the box. After propagating the wave for a time τ_A, we measured its speed. Our equations yield the phase speed V_p of an Alfvén wave:

$$V_p = V_A\sqrt{1 - 4\pi\frac{P_{||} - P_{\perp}}{B^2}} \equiv V_A\alpha, \tag{2.19}$$

where $\alpha = \sqrt{1 - 4\pi(P_{||} - P_{\perp})/B^2}$. This result is identical to that from the Chew-Goldberger-Low (CGL) equations since in the linear limit of the system the pressure remains unperturbed. In Figure 2.1 the wave phase speed V_p is plotted as a function of the anisotopy parameter α. The agreement with linear wave theory is excellent.

In our second benchmark we explored the linear growth of the firehose instability with an imposed initial unstable pressure anisotropy with $\alpha^2 = -0.16$. We initialized the simulation with small sinusoidal perturbations for 18 values of the wavenumber, $k = m/2\pi L$, where $m = 1, 2, ...$ is the mode number, and the viscosity was $\nu = 6.0 \cdot 10^{-5}$. The theoretical growth rate is given by $\gamma = kV_A|\alpha| - \nu k^4$. The viscosity controls the cutoff of the instability at short spatial scales. In Figure 2.2 we plot the theoretical (solid red line) and numerical growth rates (black stars) for the range of unstable wave numbers. For $m > 18$ the modes are stable. There is excellent agreement between the new model and what one would expect from linear

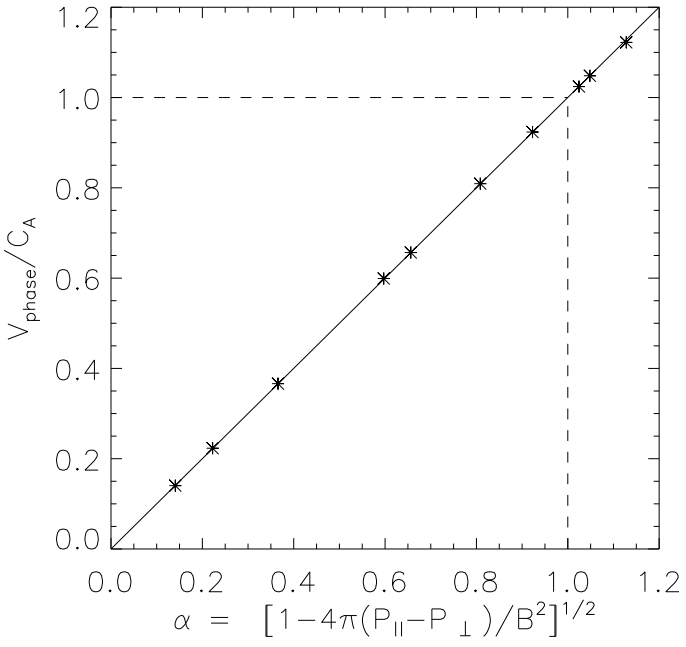

Figure 2.1: For each of ten simulations we plot the measured phase speed of the Alfvén wave V_p versus the anisotropy parameter α. The solid line is what we expect from our model, which is the same as that of the linearized CGL equations. The dotted lines show where the isotropic Alfvén wave lies and separates the region where $P_{||}$ is greater than $P_{\perp}$ from where it is smaller.

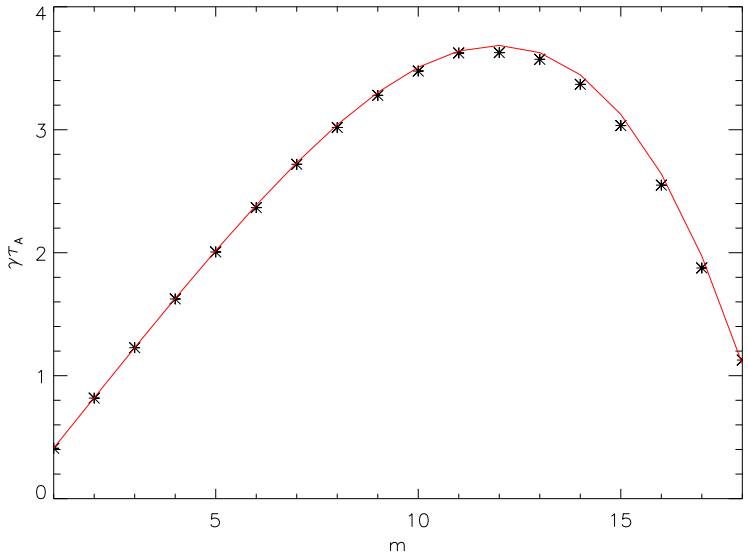

Figure 2.2: Normalized growth rate, $\gamma\tau_A$, verus the mode number, $m = 2\pi kL$, for a range of unstable values of m. The numerically determined values of $\gamma\tau_A$ are marked with black stars and the theoretical growth rate as a red line.

theory.

2.3 Summary and Discussion

The enormous separation between kinetic scales (the Debye length, the electron and ion inertial scales and Larmor radii) in the solar corona (as small as a centimeter) and the energy release scales (10^4km), mean that modeling the release of energy in flares in the solar corona and other astrophysical systems using a PIC model, which needs to resolve the Debye scale, is not feasible even with projected increases in computational power. Recent advances in our understanding of the mechanisms for particle acceleration [15, 16], suggest that these boundary layers,

which control the structure of parallel electric fields, play only a minor role in the production of the most energetic particles. Particle acceleration is controlled by the large-scale dynamics of magnetic fields through the merging of magnetic islands in 2D systems and the turbulent interactions of x-lines in the more physically realistic 3D systems. We have presented here a new model in which we have ordered out all of the relevant kinetic boundary layers. The result is a model that is scale independent and therefore capable of modeling macroscale systems.

The model consists of an MHD backbone in which macroparticles (electrons) move through the MHD grid using the guiding center equations with electric and magnetic fields given by the usual MHD prescription. Importantly, the energetic electrons feed back on the MHD fluid through the perpendicular currents associated with their anisotropic stress tensor. The consequence is that energy is conserved exactly. Further the development of pressure anisotropy of the energetic component (with $P_{||} > P_{\perp}$) properly describes the reduction in magnetic tension that drives reconnection and therefore controls the feedback of the energetic particles on the dynamics of reconnection. The equations describing the full system consist of Eqns. (2.7)-(2.17) with the energy conservation relation given in Eqn. (2.18). A code has been developed to solve these equations by merging the basic algorithms of the *f3D* Hall MHD and *p3d* PIC codes. The resulting model has been benchmarked with the propagation of Alfvén waves and firehose modes in a system with a specified initial pressure anisotropy.

In the following chapters we describe how the addition of a large-scale parallel electric field can develop as a result of electron pressure gradients in reconnecting

systems [31,32,34]. Both electrons and ions are heated as they enter the reconnection exhaust. Because the thermal motion of electrons is so much greater than that of the ions, especially for mass-ratios that approach realistic values, electrons try to escape on the reconnected field lines threading the exhaust, which extend into the upstream plasma that has not yet entered the exhaust. Charge neutrality, of course, prevents the electrons from streaming upstream and the result is a parallel potential that traps electrons in the exhaust. This potential is not large enough to significantly impact the most energetic electrons in the system. However, electrons that first enter the exhaust drop down the potential and boost their parallel velocity. This energy increase facilitates subsequent energy gain through Fermi reflection [32, 34]. The parallel electric field associated with the charge neutrality constraint can be calculated from the electron parallel force balance, obtained from the sum of the electron momentum equations ((2.2) and (2.3)) projected along the magnetic field direction with the total inertia of the electrons neglected [34]. The resulting expression for $E_{||}$ is given by

$$E_{||} = -\frac{1}{ne}\left(\mathbf{b}\cdot\nabla P_{ec} + \mathbf{B}\cdot\nabla\frac{m_e n_{ec} v_{ec||}^2}{B} + \mathbf{b}\cdot(\nabla\cdot\mathbb{T}_{eh})\right). \tag{2.20}$$

Note that the individual streaming velocities of the cold and hot electrons and their associated inertias could be large but the constraint on the total parallel current requires that the sum of the streaming velocities be small. This is a traditional return current picture in which hot electrons stream outwards from a region where magnetic energy is being released but drive a return current of cold electrons that eliminates the net electron current and prevents charge separation of the two species.

The physics argument leading to Eq. (2.20) is similar to that presented by Kulsrud to calculate $E_{||}$ [62]. He argued that the parallel electic field would develop to maintain charge neutrality in the system. His expression for $E_{||}$ includes corrections associated with ion dynamics, which are of order m_e/m_i smaller than those retained in Eq. (2.20). In our model the Debye length is ordered out so the system must remain charge neutral. The ion density is calculated with a standard continuity equation with a velocity given by the MHD momentum equation. The energetic electron density is calculated by mapping the energetic electrons onto the MHD grid with an appropriate interpolation scheme. The cold electron density is then calculated by requiring that the sum of the cold and hot electron densities match that of the ions. The physics leading to charge neutrality is the strong parallel motion of the cold electrons that fills in for the hot electrons motion along the ambient magnetic field.

Thus, our goal is to extend the present model by incorporating the parallel electric field into the equations and then to proceed with a comparison of electron heating in simple 2D reconnecting systems using the new model and standard PIC.

Chapter 3: Large-Scale Parallel Electric Fields and Return Currents in a Global Simulation Model

In this chapter we discuss the addition of a large-scale parallel electric field. This electric field plays an important role in nonthermal electron gain by preventing low energy electrons undergoing acceleration in the reconnection exhausts from escaping, allowing them to receive multiple Fermi kicks and therefore gain energy more rapidly. We develop the equation describing this parallel electric field and test its properties by measuring the speed and damping rate of electron acoustic modes and comparing with analytic results based in linear kinetic theory. These modes mediate the interplay between the fast electrons leaving the reconnection exhaust and the cold electron return current. The material in this chapter has been adapted from [74] with permission from the authors.

3.1 The *kglobal* model with $E_{||}$

Since the parallel electric fields that develop in kinetic scale boundary layers [57,58] are ineffective drivers of energetic electrons during reconnection [16,27,28], we have formulated a model in which all kinetic scale boundary layers are eliminated [23]. This new model includes the key physics necessary to produce high

energy particles without having to resolve kinetic scales. We do this by representing hot electrons as particles and cold electrons and ions as an MHD fluid. The hot electrons are evolved using the guiding center equations and they feed back on the fluid through their gyrotropic pressure tensor in the ion momentum equation. The electric and magnetic fields are evolved in the usual way from the MHD fluid. [23] presented in detail the derivation of this model. Crucially, this model conserves energy, which prevents the electron energy from running away. The dominant feedback is through the development of pressure anisotropy of the energetic electrons – a strong increase of the parallel electron pressure weakens the magnetic tension that drives reconnection, thereby throttling magnetic energy release. MHD codes are able to achieve normalized rates of reconnection that are of the order of 0.01 through the formation of multiple plasmoids. This rate is smaller than typical rates from PIC simulations [52, 75]. However, through the introduction of artificial resistivity and hyperviscosity fast rates of reconnection can be achieved in the MHD model [76]. Care must be taken, however, that artifical dissipation does not suppress multi, x-line reconnection, which is required to produce a non-thermal particle spectrum. Our plan is to explore various approaches to achieve fast reconnection while minimizing the impact on multi x-line formation. We should be able to correctly capture the physics of the acceleration of suprathermal electrons in a macroscale system with none of the constraints associated with including kinetic-scale boundary layers – there are no kinetic-scale boundary layers in the model. This *kglobal* code is operational and preliminary tests of its capabilities have been described in [23]. It correctly describes an Alfvén wave in the presence of a pressure anisotropy and

reproduces the linear growth rate of the firehose instability.

The large-scale parallel electric field is obtained by combining the parallel momentum equations for the three species (ions, cold electrons and hot electrons) into a single equation for the total parallel current. Because of constraints on this current, the driver of the current must be small and therefore can be set to zero, which yields a constraint equation for the parallel electric field. The details of the calculation are shown in the Appendix of this chapter 3.4. The resulting expression for the parallel electric field is given by

$$E_{||} = \frac{-1}{n_i e}\left(\mathbf{B}\cdot\nabla\left(\frac{m_e n_c v_{||c}^2}{B}\right) + \mathbf{b}\cdot\nabla P_c + \mathbf{b}\cdot\nabla\cdot\mathbf{T}_h\right) \tag{3.1}$$

where m_e is the electron mass, n_c, n_h, $n_i = n_c + n_h$, $v_{||c}$, $v_{||h}$, and $v_{||i}$ are the densities and flow speeds (parallel to the magnetic field) of the two electron species and the ions respectively, P_c is the scalar pressure of the cold electron fluid, B is the magnetic field, $\mathbf{b}$ is a unit vector along $\mathbf{B}$, and $\mathbf{T}_h$ is the gyrotropic stress tensor of the hot electron particles, including their inertial contributions [23],

$$\mathbf{T}_h = T_{eh||}\mathbf{bb} + P_{eh\perp}(\mathbf{I} - \mathbf{bb}), \tag{3.2}$$

where $\mathbf{I}$ is the unit tensor, $T_{eh||}$ is the stress tensor along the magnetic field $\mathbf{B}$ and $P_{eh\perp}$ is the usual perpendicular pressure,

$$P_{eh\perp} = \int d\mathbf{p}_e \frac{p_{e\perp}^2}{2m_e\gamma_e} f, \tag{3.3}$$

where in the frame drifting with $\mathbf{v_E} = c\mathbf{E}\times\mathbf{B}/B^2$ there are no perpendicular flows so $f = f(\mathbf{x}, p_{e||}, p_{e\perp}, t)$. $T_{eh||}$ includes the mean parallel drifts of the hot electrons,

$$T_{eh||} = \int d\mathbf{p}_e \frac{p_{e||}^2}{m_e\gamma_e} f, \tag{3.4}$$

with $p_{e||}$ the hot parallel electron momentum with relativistic factor γ_e. The normalizations for *kglobal* described in [23] remain unchanged. However, we now have a separate normalization for the parallel electric field, $E_{||} \sim m_e C_{Ae}^2/eL_0 = m_i C_A^2/eL_0$ where C_{Ae} is the electron Alfvén speed, and L_0 is the length scale of the domain. The normalization for $E_{||}$ comes from parallel force balance. Compared with the usual scaling for the perpendicular electric field $\mathbf{E}_\perp \sim C_A B_0/c$, the parallel electric field satisfies $E_{||}/E_\perp \sim d_i/L_0 \ll 1$. Thus we only keep the parallel electric field for motion along the field lines and it can therefore be neglected in Faraday's equation when evolving the magnetic field. The addition of this electric field modifies the momentum equation for the ions and the guiding center equation for the particle electrons from [23] in the following way:

$$\rho\frac{d\mathbf{v}}{dt} = \frac{1}{c}\mathbf{J}\times\mathbf{B} - \nabla P_i - \nabla_\perp P_c - (\nabla\cdot\mathbf{T}_{eh})_\perp + en_iE_{||}\mathbf{b} - m_e n_c v_{||c}^2\kappa \quad (3.5)$$

$$\frac{d}{dt}p_{e||} = p_{e||}\mathbf{v_E}\cdot\kappa - \frac{\mu_e}{\gamma_e}\mathbf{b}\cdot\nabla B - eE_{||} \quad (3.6)$$

where $\kappa = \mathbf{b}\cdot\nabla\mathbf{b}$ is the magnetic curvature and $\mu_e = p_{e\perp}^2/2m_eB$ is the magnetic moment of the electron. Note that in Eq. (3.5) the gradients of the cold electron pressure and hot electron stress tensor are now in the perpendicular direction only. See the Appendix of this chapter 3.4 for a derivation of Eq. (3.5). Since the parallel electric field is the same order as the pressure terms in Eq. (3.5), thermal particles are reflected by this electric potential, which prevents heated electrons from escaping from the reconnection diffusion region and the exhaust [32,34]. The consequence for electrons is that they can undergo multiple Fermi reflections within the reconnection exhaust, which facilitates the initial energy gain of electrons.

With the inclusion of a large-scale parallel electric field, *kglobal* should correctly describe the dynamics of hot electrons escaping along the ambient magnetic field in an open system and the development of a return current of cold electrons. The large-scale parallel electric field suppresses the escape of hot electrons and drives a return current of cold electrons. In its most basic form this dynamic can be reduced to that of an electron acoustic mode, which can exist in plasmas with separate and distinct electron populations [77]. In the electron acoustic mode the electrons slosh back and forth on a short time scale so that the ions are practically stationary. Thus, we benchmark *kglobal* by simulating this process.

3.2 Testing

Since electron acoustic waves only involve electron motion parallel to the magnetic field, the only non-zero gradients are along the magnetic field. Thus, the perturbed distribution function, $\tilde{f}$, of the hot electrons is only a function of $v_{||}$ and $x_{||}$. We obtain

$$\partial_t \tilde{f} + v_{||}\nabla_{||}\tilde{f} - \frac{e}{m_e}\tilde{E}_{||}\partial_{v_{||}} f_0 = 0. \tag{3.7}$$

Similarly, by enforcing charge neutrality and taking the cold electron pressure from the constancy of $P_c/n_c^{5/3}$, Eq. (3.1) becomes

$$\tilde{E}_{||} = -\frac{1}{n_i e}\left(\frac{5}{3}\nabla_{||}T_c\tilde{n}_h + \nabla_{||}\tilde{T}_h\right). \tag{3.8}$$

By assuming that the unperturbed hot electron distribution function is a Maxwellian, we can solve Eq. (3.7) for $\tilde{f}$ and take the moments to obtain the first order corrections to the hot electron density and pressure. After some algebra the dispersion

function for the electron acoustic wave is:

$$\frac{n_{0c}}{n_{0h}} = Z'(\zeta)\left(\frac{5}{6}\frac{T_{0c}}{T_{0h}} - \zeta^2\right) \tag{3.9}$$

where n_{0c} is the unperturbed density of the cold electrons (fluid), n_{0h} is the unperturbed density of the hot electrons (particles), T_{0c} is the unperturbed temperature of the cold electrons, T_{0h} is the unperturbed temperature of the hot electrons, $\zeta = \omega/kv_{th}$, v_{th} is the thermal speed of the hot electrons, and $Z'(\zeta)$ is the derivative of the plasma dispersion function. Note that this result matches that of [77] in the long wavelength limit $k \ll k_{De}$ where k_{De}^{-1} is the Debye length. For $T_{0c} \ll T_{0h}$ and $n_{0c} \ll n_{0h}$ the phase speed of the wave is small compared with v_{th} and the mode is only weakly damped and has a characteristic frequency

$$\omega = kv_{th}\sqrt{\frac{n_{0c}}{n_{0h}} + \frac{5}{6}\frac{T_{0c}}{T_{0H}}}. \tag{3.10}$$

We numerically solved this equation for various values of the density and temperature ratios and obtained the frequency and decay rates of these waves. For each value of the two parameters, we initialized *kglobal* with a sinusoidal perturbation in the electron density and temperature and measured the corresponding frequencies and decay rates of the resulting disturbance. The results of the linear theory and the simulation results are plotted in Fig. 3.1. The damping rate of the mode is controlled by the Landau resonance with the energetic component which is accurately captured by the code, a remarkable result. A similar argument can show that *kglobal* can damp ion acoustic waves with Landau damping as well.

In our final test we compare a simulation with *kglobal* to a simulation with the PIC code *p3d* [73]. We set up a simplified version of what we expect to see in a

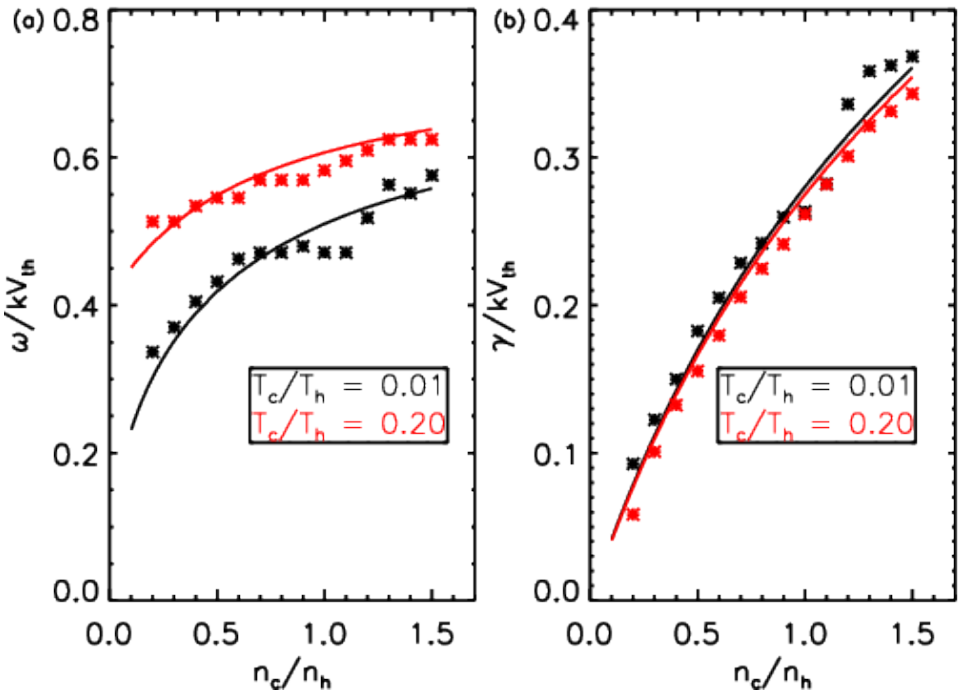

Figure 3.1: In panel (a) the electron acoustic wave phase speed versus the cold to hot density ratio of the electrons. In panel (b) the electron acoustic wave damping rate versus the cold to hot density ratio of the electrons. The stars are taken from the simulations and the lines are from the linear theory. Note that the phase speed is normalized to the thermal speed of the hot electrons and the damping rate is normalized to the time a thermal particle requires to travel one wavelength.

reconnection exhaust. The initial conditions consist of a constant magnetic field, a constant density made up of 75% particle electrons and 25% fluid electrons, and a temperature profile for the particle electrons that increases sharply in the center to twenty times the asymptotic value as can be seen in Fig. 3.2(a). This value of the hot to cold electron density ratio was chosen to quicken the dynamics since we know from Fig. 3.1(b) that the larger the ratio the larger the damping rate. To convert this setup to a PIC version, we had to make sure that the smallest length scale in *kglobal* was much larger than the Debye length since this scale is not resolved in *kglobal*. Thus we equated the transition width between the two regions of hot and cold electrons to 30 times the Debye length.

In both simulations we utilized a large spatial domain in the parallel direction so there is space for the hot electrons to expand. A small domain in the perpendicular direction was included so that the data could be averaged over this direction to decrease particle noise. For *kglobal* we had a domain of 2048 x 64 cells and for *p3d*, 8192 x 64. In both simulations the electron to ion mass ratio was 1/1836 and the speed of light was 300 times the Alfvén speed. For *p3d* a uniform background with constant density and a temperature corresponding to the cold electron fluid in *kglobal* was included along with an electron population with the same temperature profile as the hot species in *kglobal*. The results from these simulations are shown in Fig. 3.2. The PIC simulation is in solid black, *kglobal* is in red, and the result from *kglobal* without a parallel electric field is in dashed red. We added the latter so we could determine how the addition of the parallel electric field influenced the dynamics. First, the temperature profiles from *p3d* and *kglobal* with $E_{||}$ match very

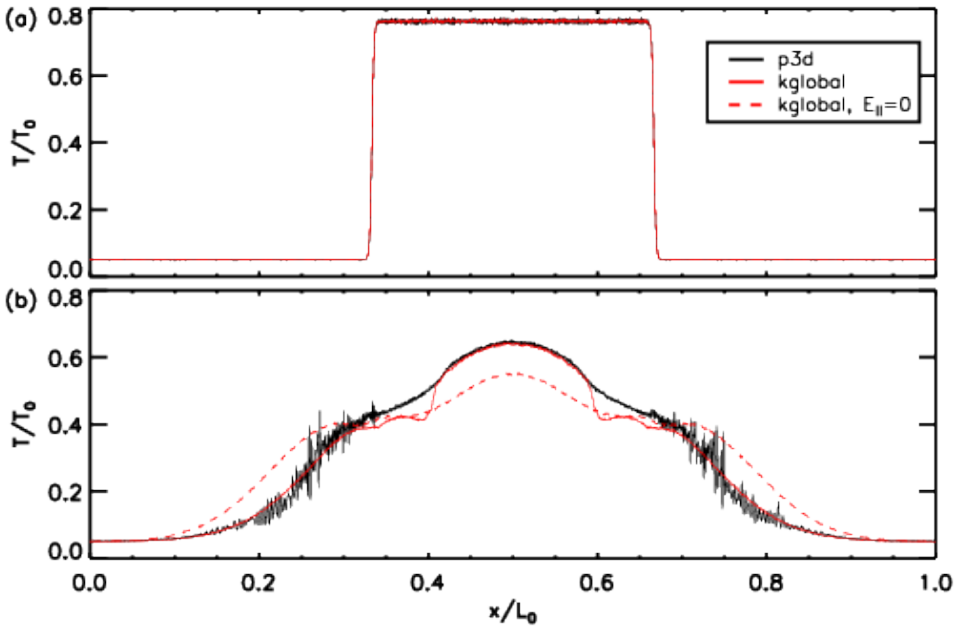

Figure 3.2: Profiles of the total electron temperature for the PIC code *p3d* (black), the *kglobal* code with the included parallel electric field (red) and without the parallel electric field (dashed red). In panel (a) at $t/t_{th} = 0$. In panel (b) at $t/t_{th} = 0.12$ where t_{th} is the time a hot thermal electron requires to travel the length of the box.

well over most of the domain. In contrast, the temperature in *kglobal* with $E_{||} = 0$ spreads much more rapidly, demonstrating that $E_{||}$ does inhibit electron thermal transport and that the the model for $E_{||}$ in *kglobal* correctly describes transport suppression.

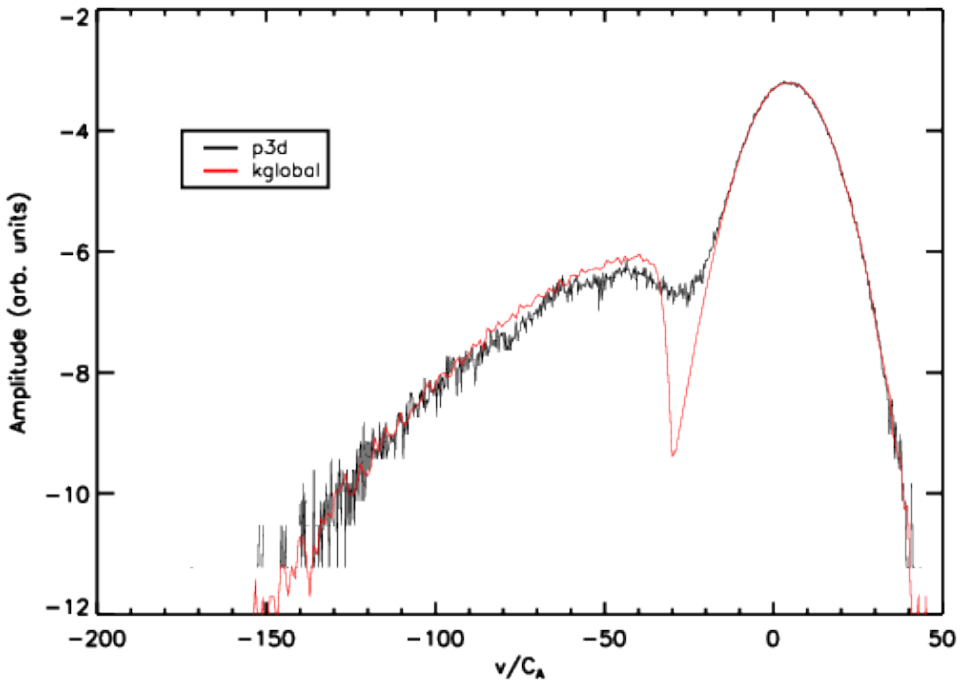

Figure 3.3: The log of the particle distribution functions from the PIC code *p3d* (black) and the *kglobal* code (red) taken at $x/L_0 = 0.25$. Notice the dip in the *kglobal* distribution function around $v/C_A = -30$.

While *kglobal* is able to capture the overall dynamics of the temperature profile, it does not produce the short scale spatial oscillations seen in the *p3d* data. These oscillations are plasma waves driven unstable by a bump-on-tail velocity distribution that smooths out the plateaus in the temperature visible in the *kglobal* data around $0.3 < x/L_0 < 0.4$ and $0.6 < x/L_0 < 0.7$. Fig. 3.3 displays the distribution functions

from *p3d* in black and from *kglobal* in red at $x/L_0 = 0.25$ at the time shown in Fig. 3.2 panel (b). Note that for *kglobal* a Maxwellian with density and temperature equal to that of the cold electron fluid was added to the hot electron distribution function so that we could directly compare cuts to *p3d*. There is a sharp dip visible in the velocity distribution from *kglobal* around $v/C_A = -30$ that is not seen in the data from *p3d*. In the *p3d* simulation, the faster particles have lost energy to plasma oscillations and filled in this dip, forming a plateau in phase space. This result is not seen in the *kglobal* data because this model does not support plasma waves, which require a violation of charge neutrality to exist. Electron sound waves can be driven unstable by structures in velocity space, but the phase speed of these waves is fixed by the local plasma parameters (see Eq. (3.9)) and so will typically not be resonant with electrons in the bump region shown in Fig. 3.3.

3.3 Conclusion

The *kglobal* code [23] has been upgraded to include a macroscale $E_{||}$ that develops as a result of gradients in the plasma pressure parallel to the ambient magnetic field. The upgraded model now captures the dynamics of electron acoustic waves and accurately describes the suppression of transport of hot electrons parallel to the ambient magnetic field, a process that is important in the early phases of electron acceleration in magnetic reconnection [33, 34]. The inclusion of the large scale $E_{||}$ is also important in describing the development of return currents that form as hot electrons escape from regions of electron acceleration in macroscale energy

release events such as flares in the solar corona. This new capability combined with the ability of the model to describe the impact of pressure anisotropy on magnetic field dynamics (e.g., firehose instability), which is critical for describing the feedback of energetic particles on reconnection dynamics, suggest that the *kglobal* code can be used to accurately simulate nonthermal electron acceleration during magnetic reconnection.

Our next step is to begin to explore the energization of electrons during magnetic reconnection with *kglobal* and to determine whether the reconnection dynamics in a macroscale system can produce the power-law distributions that are ubiquitous in observations [65, 70]. Because *kglobal* is a macroscale model, the dynamics of particle acceleration can be explored in a much larger domain than with a traditional PIC model. In addition, we will include particle loss in a realistic manner to establish whether or not it is the balance between reconnection drive and the escape of energetic particles that leads to powerlaw distributions [30, 78]. Finally, in a macroscale simulation model the inclusion of a synthetic diagnostic to describe synchrotron emission and bremsstrahlung emission will be possible.

3.4 Appendix

3.4.1 Energy Conservation

We start with the momentum equations for the three species, the ions

$$\rho \frac{d\mathbf{v}_i}{dt} = ne\mathbf{E} + \frac{ne}{c}\mathbf{v}_i \times \mathbf{B} - \nabla P_i, \tag{3.11}$$

the cold electrons

$$\frac{\partial(m_e n_c v_{||c}\mathbf{b})}{\partial t} = -n_c e\mathbf{E} - \frac{n_c e}{c}\mathbf{v}_c \times \mathbf{B} - \nabla P_c \\ - \mathbf{bB}\cdot\nabla\frac{m_e n_c v_{||c}^2}{B} - m_e n_c v_{||c}^2\kappa \quad (3.12)$$

and the hot electrons

$$\frac{\partial(m_e n_h \bar{v}_{||h}\mathbf{b})}{\partial t} = -n_h e\mathbf{E} - \frac{n_h e}{c}\bar{\mathbf{v}}_h \times \mathbf{B} - \nabla\cdot\mathbf{T}_h, \quad (3.13)$$

where ρ and $\mathbf{v}$ are the ion mass density and velocity, from charge neutrality $n = n_c + n_h$ and the electron inertia has only been retained in the direction along the ambient magnetic field. In writing the electron momentum equations we have for simplicity assumed that the mean drifts of both species are not relativistic. The individual electron fluxes can be of order nC_{Ae} while the ion flux is of order nC_A. However, we show below that the total current is much smaller than the contribution from each species of particle and this yields a constraint on the total driver of the current. To see this we divide the momentum equations along the field lines by their respective masses and subtract Eqs. (3.12) and (3.13) from Eq. (3.11), which yields

$$\frac{1}{e}\frac{\partial J_{||}}{\partial t} = \frac{n_i e E_{||}}{m_e} + \mathbf{b}\cdot\left(\frac{1}{m_e}\nabla P_c + \frac{1}{m_e}\nabla\cdot\mathbf{T_h}\right) + \mathbf{B}\cdot\nabla\left(\frac{n_c v_{||c}^2}{B}\right) \quad (3.14)$$

All of the terms on the right hand side of this equation act as drivers of $J_{||}$. However, the parallel current driven is constrained by the structure of the magnetic field which is produced by this current. This constraint follows from Ampère's law $J_{||} \sim cB/4\pi L$, where L is the macroscopic characteristic perpendicular scale of the magnetic field. Comparing the time derivative of this current, given by c_A/L, with

the characteristic scaling of the terms on the right, *e.g.*, the gradient of the hot thermal electrons, which scales as $n_h T_h/m_e L$, we find that the ratio of the left to the right side of the equation scales like $\sqrt{m_e/m_i}(d_e/L) \ll 1$. Thus, the time derivative of the current can be discarded. This tells us that

$$v_{||c} = \frac{1}{n_c}(n_i v_{||i} - n_h v_{||h}). \tag{3.15}$$

Note that this constraint equation for $v_{||c}$ includes the ion motion. That the ions must also be included in the constraint follows because the mean drift speed associated with the current (from the previous scaling for $J_{||}$) scales like $nC_A(d_i/L) \ll nC_A$, the characteristic current carried by the ions. This constraint on the parallel flows is consistent with the conclusions of [62] and yields the equation for $E_{||}$ in Eq. (3.1). If the mean flows of the electrons becomes relativistic, corrections to Eq. (3.1) of order $v_{||h}/c$ must be included.

A further consequence of this result is that the sum of the fluxes of the two electron species is limited to a scale of the order of the ion flux. The consequence is that when the three momentum equations are summed, the electron inertia arising from the time derivative can be discarded, which yields the ion momentum equation,

$$\rho\frac{d\mathbf{v}}{dt} = \frac{1}{c}\mathbf{J}\times\mathbf{B} - \nabla(P_i + P_c) - \nabla\cdot\mathbf{T}_{eh} - \mathbf{bB}\cdot\nabla\frac{m_e n_c v_{||c}^2}{B} - m_e n_c v_{||c}^2\kappa, \tag{3.16}$$

which is equivalent to the form shown in Eq. (3.5). To explore energy conservation of Eqs. (3.5) and (3.6) along with the usual fluid equations, we take the dot product

of Eq. (3.5) with $\mathbf{v}$ and use the ion continuity equation to obtain

$$\frac{\partial}{\partial t}\frac{\rho v^2}{2} + \nabla \cdot \frac{\rho \mathbf{v} v^2}{2} + \mathbf{v} \cdot \nabla P_i = (\mathbf{J}_\perp - \mathbf{J}_{\perp c} - \mathbf{J}_{\perp h}) \cdot \mathbf{E}_\perp$$
$$- (J_{||c} + J_{||h}) E_{||} = \mathbf{J}_\perp \cdot \mathbf{E}_\perp - (\mathbf{J}_c + \mathbf{J}_h) \cdot \mathbf{E}, \quad (3.17)$$

where we have used the perpendicular components of Ohm's law $\mathbf{E}_\perp = -\mathbf{v} \times \mathbf{B}/c$, the perpendicular components of the two electron momentum equations and Eq. (3.15) for $v_{||c}$. From Faraday's law we find

$$\frac{\partial}{\partial t}\frac{B^2}{8\pi} + \frac{c}{4\pi}\nabla \cdot (\mathbf{E} \times \mathbf{B}) + \mathbf{J}_\perp \cdot \mathbf{E}_\perp = 0, \quad (3.18)$$

which, when combined with Eq. (3.17), yields the conservation law

$$W_{MHD} + W_c + W_h = constant, \quad (3.19)$$

where we have discarded terms corresponding to the divergence of the various energy fluxes. The MHD energy, W_{MHD}, includes the ion bulk kinetic and thermal energies and the magnetic energy, the cold electron energy includes both the kinetic energy associated with parallel streaming and the thermal energy,

$$W_c = \frac{m_e n_c v_{||c}^2}{2} + \frac{1}{\Gamma - 1} P_c \quad (3.20)$$

with Γ the ratio of specific heats. The hot electron energy is the sum of the parallel kinetic energies of all hot electrons as well as the energy associated with their perpendicular gyro motion. It does not include the kinetic energy associated with the perpendicular bulk flow, which is negligible.

Chapter 4: Electron Acceleration during Macroscale Non-Relativistic Magnetic Reconnection

In this chapter we discuss results from simulations of 2D magnetic reconnection with the *kglobal* model and compare with observations of solar flares, specifically focusing on a flare that took place on September 10, 2017, that was well-diagnosed by remote observations from multiple spacecraft and ground-based facilities [70,79–81]. Magnetic reconnection is facilitated by including a hyper-resistivity in Faraday's law. Reconnection starts from particle noise and proceeds to produce multiple small islands that merge into larger islands and accelerate electrons. Fermi reflection is responsible for accelerating electrons to nonthermal energies. We show, however, that a strong guide field drastically suppresses the production of these nonthermals. This is because the guide field reduces the curvature of the magnetic field. We present an analytic model that describes electron energy gain in a finite-length current layer with merging magnetic islands and convective loss. The spectral indices that result from this model, including the dependence on the guide field, compare favorably with results of *kglobal* simulations. Further, we evaluate the number density of nonthermal electrons and their integrated energy content and the number density of hot thermal electrons and their temperature increment versus guide field and

system size. Large guide field simulations produce almost no nonthermal electrons. In contrast, the temperature increment of the hot thermal electrons is relatively insensitive to the guide field. Finally, we carry out a detailed comparison between the predictions of *kglobal* and the observations of the September 10, 2017, solar flare. The material in this chapter has been adapted from [82] with permission from the authors.

4.1 Numerical Simulations Setup

The 2D simulations presented here are carried out with the *kglobal* model, which consists of a magnetohydrodynamic (MHD) backbone with fluid ions and electrons as well as particle electrons that are distributed as macroparticles on the MHD grid. The two electron species combine so that charge neutrality is preserved at all times [23, 74]. However, since the equations governing energy gain in the electron fluid are incomplete (e.g., Fermi reflection is not included), any change in the energy of the electron fluid will be neglected in the analysis of the electron energy gain. The upstream reconnection magnetic field, B_0, and the ion density, n_0, define the Alfvén speed, $C_{A0} = B_0/\sqrt{4\pi m_i n_0}$. Since no kinetic scales are resolved, lengths are normalized to an arbitrary macroscale L_0. Times are normalized to $\tau_A = L_0/C_{A0}$ and temperatures and particle energies to $m_i C_{A0}^2$. The perpendicular electric field follows an MHD scaling, $C_{A0}B_0/c$. The parallel electric field scales like $m_i C_{A0}^2/L_0 e$ and is small compared with the perpendicular component. However, the energy associated with the parallel potential drop acting over the scale L_0 is of

order $m_i C_{A0}^2$, which is comparable to the available magnetic energy per particle.

The simulations are initialized with constant densities and pressures in a force-free current sheet and periodic boundary conditions. Thus, $\boldsymbol{B} = B_0 \tanh(y/w)\hat{\boldsymbol{x}} + \sqrt{B_0^2 + B_g^2 - B_0^2 \tanh^2(y/w)}\hat{\boldsymbol{z}}$. The temperatures of all three species are uniform and isotropic with $T_i = T_{e,part} = T_{e,fluid} = 0.0625 m_i C_{A0}^2$, leading to an initial plasma β of 0.25 (based on B_0). While the initial β is higher than typical coronal values, electron heating and acceleration is insensitive to this choice as well as to the chosen fraction of particle electrons (25% of the total electrons). The domain size for all simulations is $L_x \times L_y = 2\pi L_0 \times \pi/2L_0$. The magnetic field evolution equation includes a hyper-resistivity ν to facilitate reconnection, while minimizing dissipation at large scales [83]. The effective Lundquist number $S_\nu = C_A L_0^3/\nu$ associated with this hyper-resistivity is varied to change the effective system size (ratio of the macro to the dissipation scale). We also include fourth and second order viscosity terms and some electron particle diffusion to prevent a numerical instability associated with trapping electrons in small perpendicular electric field fluctuations. Reconnection begins from particle noise and proceeds to produce multiple flux ropes whose number depends on S_ν, with larger values of S_ν producing more initial flux ropes. However, our late-time results are relatively insensitive to S_ν and therefore the effective system size. Thus, unless otherwise stated we focus on simulations with $N_x \times N_y = 2048 \times 512$ grid cells, 100 particles per cell, time step $dt = 0.0001\tau_0$ and $S_\nu = 9.5 \times 10^7$. The mass ratio is $m_i/m_e = 25$. The results are not sensitive to this value. The speed of light is $c/C_{A0} \approx 60$. We use guide fields $B_g/B_0 = 0.1$, 0.25, 0.4, 0.5, 0.6, 0.8, and 1.0.

4.2 Simulation Results

Since magnetic reconnection in our simulations is triggered by particle noise, the dynamics begins with the growth of many small islands, which subsequently undergo mergers and eventually approach the system scale. This behavior is seen in Fig. 4.1 from a simulation with $B_g/B_0 = 0.25$. The energy per particle of the particle electrons, $< W >$ (energy density divided by number density), is shown in the $x-y$ plane at three times, $t/\tau_A = 2.5$, 5, and 8 in panels (a), (b), and (c). Magnetic field lines are superimposed. The particle electron energy is nearly constant along field lines because of the high electron mobility parallel to the magnetic field.

The firehose parameter, $1 - (P_{||} - P_{\perp})/4\pi B^2$, is plotted in Fig. 4.1(d) at late time from a simulation with $B_g/B_0 = 0.1$. Large regions within the magnetic islands are near marginal stability (with some unstable regions) so that the local magnetic tension, which drives particle energy gain, is largely suppressed within flux ropes in this simulation. Thus, electron feedback on the MHD fluid is essential in regimes where electron energy gain is significant. Models based on test particle dynamics neglect the feedback of particles on the dynamics and can therefore lead to runaway electron energy gain.

The spectrum of nonthermal electrons is calculated from the simulations by summing the total number of particle electrons within a specified energy range over the entire simulation domain. This ensures that we maximize the count rate of the electrons at the highest energies to improve the statistics of the measured distribution. In Fig. 4.2(a) we plot the differential electron number density $F(W) =$

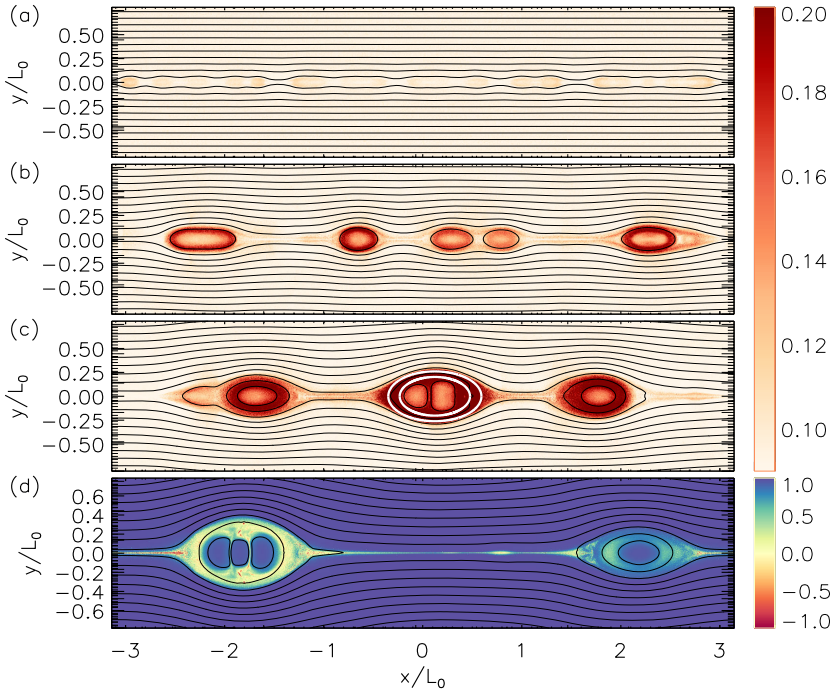

Figure 4.1: In (a), (b), and (c): $< W >$ for a simulation with $B_g/B_0 = 0.25$ in the $x - y$ plane at $t/\tau_A = 2.5$, 5, and 8 with magnetic field lines overplotted. In (d): the firehose stability parameter at late time from a simulation with $B_g/B_0 = 0.1$.

$dN(W)/dW$ versus the normalized energy, $W/m_i C_{A0}^2$, on a log-log scale at several times for the case $B_g/B_0 = 0.25$ shown in Fig. 4.1. $F(W)$ takes the form of a power-law (a straight line in the log-log plot) as time progresses. The power-law index δ' reaches a constant value at low energy early and extends to higher energy over time.

The inset in Fig. 4.2 shows the late-time $F(W)$ for several values of the guide field corresponding to times during the simulations when approximately the same amount of magnetic flux has reconnected. As the guide field decreases, δ' decreases so the spectrum becomes harder and more high-energy electrons are produced. In Fig. 4.2(b) we plot the late time spectrum of $F(W)$ for several values of S_ν. Larger values of S_ν correspond to larger systems. Thus, Fig. 4.2(b) demonstrates that the slope of the power-law of nonthermal electrons is relatively insensitive to the size of the system. However, the total energy contained in the nonthermal electrons increases with reconnected flux, and thus a larger system produces a more extended power-law.

The dependence of δ' on the guide field is plotted in the curve marked by the stars in Fig. 4.3(a). A strong guide field produces a soft nonthermal particle spectrum. The solid red curve is from the theoretical model discussed in the next section. Plotted in Fig. 4.3(b) is the time dependence of the energy of a typical electron that populates the power-law tail versus the x-position from a simulation with $B_g/B_0 = 0.25$. Early in time the electron makes several passes through the system with little change in energy. Once reconnection produces flux ropes, the electron is captured by a flux rope and, as it contracts and merges with other flux

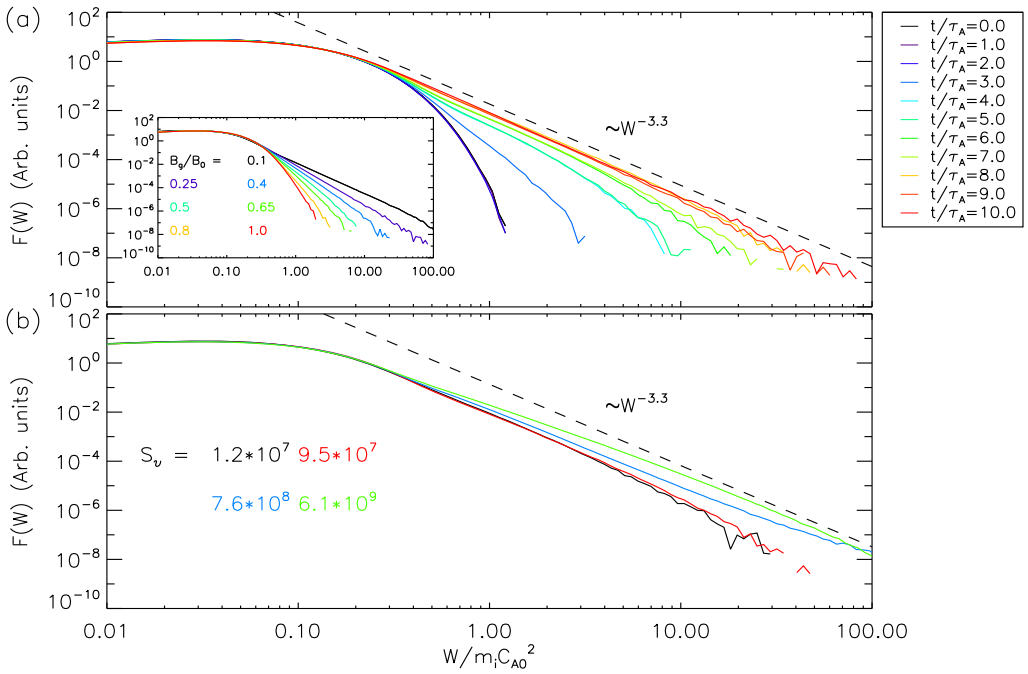

Figure 4.2: In (a): a log-log plot of $F(W)$ versus energy at multiple times for the $B_g/B_0 = 0.25$ simulation. Inset in (a): the late time $F(W)$ for several guide fields. In (b): the late time $F(W)$ for $B_g/B_0 = 0.25$ with various values of S_ν (effective system size). The dashed line in both (a) and (b) is a power-law with $\delta' = 3.3$.

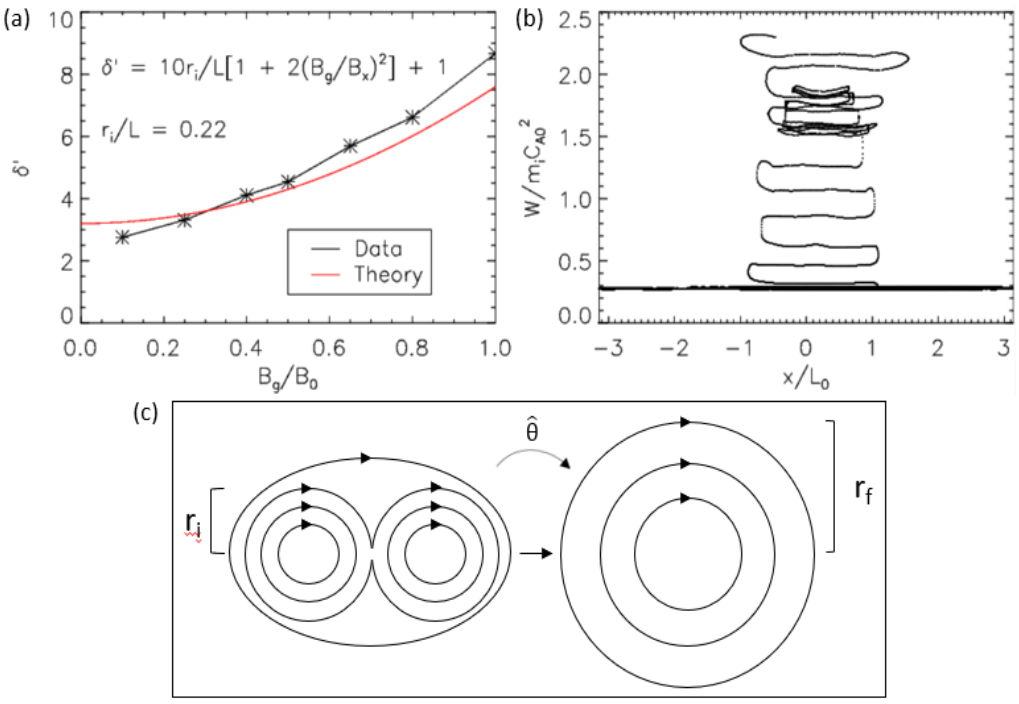

Figure 4.3: In (a): δ' (black) versus guide field and the fit from the theoretical model (red). In (b): the energy versus x position of an electron that becomes a part of the nonthermal distribution. In (c): a schematic depicting the flux rope merging mechanism that leads to electron power-law distributions.

ropes, the electron undergoes Fermi reflection, gaining energy with each bounce. Fig. 4.3(c) is a schematic of the island-merging process that leads to the power-law tail (discussed in the following section).

In exploring the power-law distribution of nonthermal electrons, we averaged over the entire computational domain to improve the statistics of the number of electrons with very high energy. However, an important question in understanding particle energy gain during reconnection concerns the relative numbers and energy content of nonthermal electrons (those in the power-law tail) versus those that dis-

play a thermal or nearly thermal distribution. The observations suggest that the nonthermals often contain more energy than the hot thermals in large flares [84–86]. To explore these questions we analyzed data from more limited spatial domains that include both hot thermal and nonthermal electrons but exclude electrons that have not yet gained energy from reconnection. We focus, therefore, on the interior of magnetic islands where the electron temperature has increased and where there are significant numbers of nonthermal electrons. The goals are to establish whether a characteristic effective temperature is associated with the hot thermal electrons and what fraction of the electrons can be categorized as hot thermal versus nonthermal.

Specifically, we explore the region between the two white ellipses within the middle flux rope in Fig. 4.1(c). In Fig. 4.4(a) we show $F(W)$ (black line) from the region between the two ellipses. The high-energy electrons form a power-law distribution even in this localized region within a single flux rope. In Fig. 4.4(b) we display the same data, but on a linear-linear scale focused on the lower energies to reveal the hot thermal population. These two plots reveal that localized regions within magnetic islands contain a mixture of electrons with a range of energies so that the characteristics of the hot thermal and nonthermals can be explored.

To model the distributions in Fig. 4.4 we use the sum of a Maxwellian and a kappa distribution. The kappa distribution fits the power-law tail of nonthermal electrons and the Maxwellian supplements the Maxwellian component of the kappa distribution at low energy, producing a good fit to the hot thermal electrons. The fitting procedure is discussed in detail in the appendix of this chapter 4.5. The outputs of the fit to the electron distribution is the spectral index of the nonthermal

electrons, and the number density and total energy content of the nonthermal and thermal electrons.

The results of fitting for all of the guide fields appear in Fig. 4.4, (c) and (d). Shown in (c) is the percentage of the total density (red) and energy (black) of the nonthermal electrons as defined in the appendix of this chapter 4.5 as a function of the guide field. Each distribution that formed the basis of this data came from a region within an island similar to the one shown in Fig. 4.1(c). For a small guide field the energy content of the nonthermal electrons is $\sim 80\%$ of the total particle electron energy and $\sim 20\%$ of the total electron particle density. As the guide field increases, the number of nonthermal electrons and their energy content becomes small. In (d) is the total energy per particle of the particle electrons (black) and the corresponding energy per particle, or $(3/2)T_{th}$, of the hot thermal electrons (red), with the initial energy shown as a dotted line. This is further evidence that the nonthermal electrons dominate the total electron energy at low guide fields where the Fermi drive is strong. On the other hand, the energy of the hot thermal electrons is relatively insensitive to the guide field and is likely controlled by slow shocks (see 4.5) rather than by Fermi reflection.

4.3 An analytic model for nonthermal electron acceleration

We present a model for electron acceleration in a current layer with merging magnetic flux ropes that captures the essential results of the *kglobal* simulations, including an expression for the power-law index of the nonthermal electrons and its

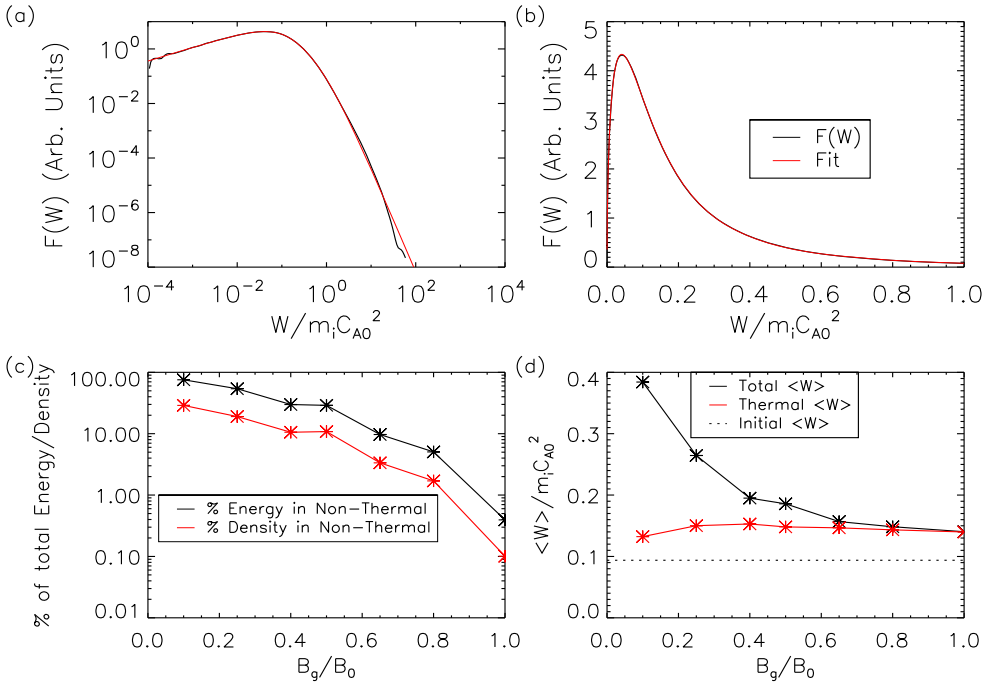

Figure 4.4: In (a): $F(W)$ (black) along with the fit (red) described in the appendix of this chapter 4.5 versus energy on a log-log scale. In (b): the same data on a linear-linear scale, zoomed in to low energies to reveal the hot thermal electrons. In (c): the percentage of energy (black) and density (red) of nonthermal electrons versus guide field. In (d): the average energy per particle of particle electrons (black) and thermal electrons (red) versus guide field. The dotted line is the energy from the initial Maxwellian distribution of particle electrons.

dependence on the ambient guide field. The model includes the convective loss of electrons injected into large, inactive flux ropes.

The model is based on electron energy gain during the merging of flux ropes. The dominant heating, parallel to the local magnetic field [16, 27], results from the shortening of field lines during flux rope mergers [30] as shown in Fig. 4.3(c): merging field lines contract from the figure-eight configuration on the left to the circle on the right. Parallel heating results from the invariance of the parallel action $\oint v_{\parallel} dl$. Thus, the change in the energy during the merger of two flux ropes can be calculated by evaluating the geometry of the magnetic field before and after the merger. The calculation presented in the appendix of this chapter 4.5, results in the rate of energy gain

$$\dot{W} = \frac{d}{dt} W = W \frac{g}{\tau_r}, \tag{4.1}$$

with $\tau_r \sim r_i / R c_{Ax}$ the merger time of a flux rope of initial radius r_i, where $R \sim 0.1$ is the normalized rate of merger of the flux ropes in the current layer, and c_{Ax} is the Alfvén speed based on the reconnecting magnetic field B_x. The factor $g = (1 + 2B_g^2/B_x^2)^{-1}$ arises from the dependence of the radius of curvature of the reconnecting magnetic field on the guide field [16, 25, 28]. With the energy gain in Eqn. (4.7), an equation can be derived for the number density $F(x, W, t)$ of electrons per unit energy undergoing reconnection-driven acceleration in a one-dimensional current layer and experiencing convective loss,

$$\frac{\partial}{\partial t} F + \frac{\partial}{\partial x} v_x(x) F + \frac{\partial}{\partial W} \dot{W} F - D \frac{\partial^2}{\partial x^2} F = \frac{1}{\tau_{up}} F_{up} \tag{4.2}$$

where $v_x(x)$ describes the convective loss of electrons as they are ejected at the

Alfvén speed out of the current layer and we include a simple constant diffusion of electrons within the current layer. The electrons are injected into the layer with an initial distribution F_{up} which is taken as a low-temperature Maxwellian. Although the simulations carried out here are periodic and particles are therefore not lost, the large flux ropes that emerge at late time and no longer participate in the reconnection process act as sinks for energetic electrons [15,87]. For a low upstream temperature and strong diffusion D, the steady state solution to Eqn. (4.2) is given by

$$F_0 \propto \frac{1}{W} W^{-c_{Ax}\tau_r/gL} \sim W^{-(1+r_i/gRL)}. \tag{4.3}$$

The energetic electron spectrum is a power-law with a spectral index that depends on the rate of reconnection R, the ratio of the characteristic radius r_i to the half-width L of the current layer and the relative strength of the guide field. A strong guide field for which $g \sim (2B_g^2/B_x^2)^{-1}$ produces a very soft electron spectrum. This scaling relation is compared with data from our simulations in Fig. 4.3(a). The best fit of the model with the data has $r_i/L = 0.22$, which is consistent with the typical scale of islands in the simulations.

4.4 Comparison with Observations

The standard model for a solar flare comes from [88]. It includes an erupting flux rope that produces a large reconnecting current sheet with a cusp-shaped flare arcade below. As reconnection proceeds, more small flux ropes are produced in the current sheet and flow either up toward the erupting flux rope, or down toward the arcade. The solar flare of September 10, 2017, was observed by several instruments

[70,79–81]. The gyrosynchrotron spectrum revealed relativistic electrons throughout the reconnecting current sheet, with an increase in intensity where the current sheet meets the arcade. The observed power-law indices, δ‘, for this region fell in the range 3.5-6.5. The RHESSI observations for this event revealed both a footpoint and an extended coronal source [70]. The coronal source had a photon spectral index near 4.4, which for thin target emission corresponds to a particle spectral index $\delta' = 3.9$. Late in the flare the temperature of the hot thermal electrons in the coronal current sheet was analyzed with the EIS Fe XXIV/Fe XXIII ratio [79]. The hot thermal electron temperature had a broad peak near 2.5keV.

Our simulations reveal that the spectral index of nonthermal electrons and the number of the nonthermals depends strongly on the ambient guide field. The September 10, 2017, flare was modeled with MHD simulations, and the magnetic field profiles in the corona were compared with those inferred from analysis of the gyrosynchrotron emission of energetic electrons [80]. MHD simulations with various guide fields produced the best agreement with a guide field that was 30% of the reconnecting magnetic field. Based on the data from Fig. 4.2, our simulations predict a power-law index near 3.5, within the range measured from gyrosynchrotron emission and very close to the RHESSI measurement.

We can also compare the temperature jump of the hot thermal electrons in our simulation with the measured 2.5keV from the EIS data. At the time the EIS data was analyzed the measured maximum outflow speed in the current sheet was $\sim$ 800km/s [89]. However, it is likely that this value is a lower bound for the Alfvén speed since flows can suffer from projection effects. Further, *in situ* measurements

at 1AU indicate that for a weak guide field the outflow speed is around 2/3 of the upstream Alfvén speed [90]. The simulation data in Fig. 4.4(d) suggests that the hot thermal electrons should have a temperature jump near $0.04 m_i C_{A0}^2$. Using 1200km/s for C_{A0}, we calculate a hot electron temperature of $0.6keV$. This is a factor of 4 smaller than the EIS measurement. Thus, further exploration of the scaling of the hot thermal temperature is needed. One possibility is that collisions thermalize the low energy nonthermal electrons thereby increasing the hot thermal temperature.

Observations of large numbers of flares have revealed that the energy in nonthermal electrons exceeds that of the thermal electrons in $\sim 80\%$ of events, suggesting that solar flares are extremely efficient at accelerating nonthermal electrons [85]. The efficiency of nonthermal electron acceleration was greatest in large flares [86] although recent evidence from NuSTAR suggests that such results might extend to smaller flares [91]. Such results are consistent with Fig. 4.4(c) for $B_g/B_0 < 0.4$. The simulations (Fig. 4.2(b) further suggest that even small flares might be efficient sources of nonthermal electrons.

4.5 Appendix

4.5.1 Electron energy gain

As has been reported in previous PIC simulations we have monitored the three mechanisms by which the particle electrons gain energy as a function of time: Fermi reflection, the parallel electric field, and betatron acceleration [27]. The data for guide fields $B_g/B_0 = 1.0$ and 0.1 are shown in Fig. 4.5(a) and (b), respectively.

As in earlier simulations, electron energy gain is bursty, which reflects the periodic merger of finite size flux ropes. In the case of a weak guide field Fermi reflection dominates energy gain during the entire simulation while acceleration by the betatron mechanism (corresponding to the conservation of the magnetic moment $V_{\perp}^2/B$) and the parallel electric field are negligible. For a strong guide field betatron acceleration is again negligible while acceleration by the parallel electric field becomes comparable to the Fermi mechanism at late time. Notably, there is an increase in heating due to $E_{||}$ toward the end of the simulation for $B_g/B_0 = 1$. This is likely due to the development of the large scale $E_{||}$ that forms after the electrons injected into the reconnection exhaust gain significant energy. At this point the resulting potential drop can heat electrons entering the exhaust as documented in PIC simulations [32, 34]. This effect is subdominant in comparison to Fermi reflection for the case of a small guide field. Note, however, that the overall electron heating rate for the strong guide field case is more than an order of magnitude lower than in the case of a weak guide field.

In Fig. 4.5(c) the parallel electric field is shown at late time. The large-scale electric field points away from the current sheet in the outflow exhausts as expected since the parallel electric field serves to prevent hot electrons from escaping upstream [32–34]. To see that the electric field points away from the current sheet, note that B_x is positive above the current sheet and negative below so that B_y is positive on the left side of the left-most flux rope. Thus, $E_{\parallel} \sim E_y$ is positive above the current sheet and negative below. The unusual vertically oriented structures in $E_{\parallel}$ correspond to the locations of slow shocks that propagate to the left and right

in the simulation. The *kglobal* model correctly describes the potential drop across the slow shock that maintains charge neutrality. The slow shocks produced during reconnection are not effective in driving the nonthermal electrons [92]. However, the electron distribution across the slow shock reveals electron reflection and acceleration that likely causes heating of the thermal electrons and leads to the thermal energy gain seen in Fig. 4(d). This heating can also be observed in the upstream region in Fig. 4.5(d), which shows the average parallel energy per particle electron and has been overexposed to show the upstream heating associated with the slow shocks. This heating process will be explored in a future paper.

4.5.2 Fitting procedure of the particle electron distributions

To model the electron distribution functions in Fig. 4 we use the sum of a Maxwellian and a kappa distribution. The functional forms of the two distributions are shown in Eqn. 4.4. Since the kappa function only has two free parameters, we include the Maxwellian component to capture the power law index, the thermal temperature, and the relative number of nonthermal electrons.

$$F_{fit}(W) = F_\kappa(W) + F_M(W) = \left[\frac{N_\kappa}{(\pi\kappa\theta^2)^{3/2}}\frac{\Gamma(\kappa+1)}{\Gamma(\kappa-1/2)}\left(1+\frac{W}{\kappa\theta^2}\right)^{-(\kappa+1)} + N_M\left(\frac{m_e}{2\pi T_M}\right)^{3/2} e^{-W/T_M}\right] 4\pi\sqrt{\frac{2W}{m_e^3}} \tag{4.4}$$

where $F_{fit}(W)$ is the fit to the total electron differential density, N_κ is the density of the kappa function, θ is the most probable speed in the kappa function, Γ is the Gamma function, N_M is the density of the Maxwellian function, m_e is the

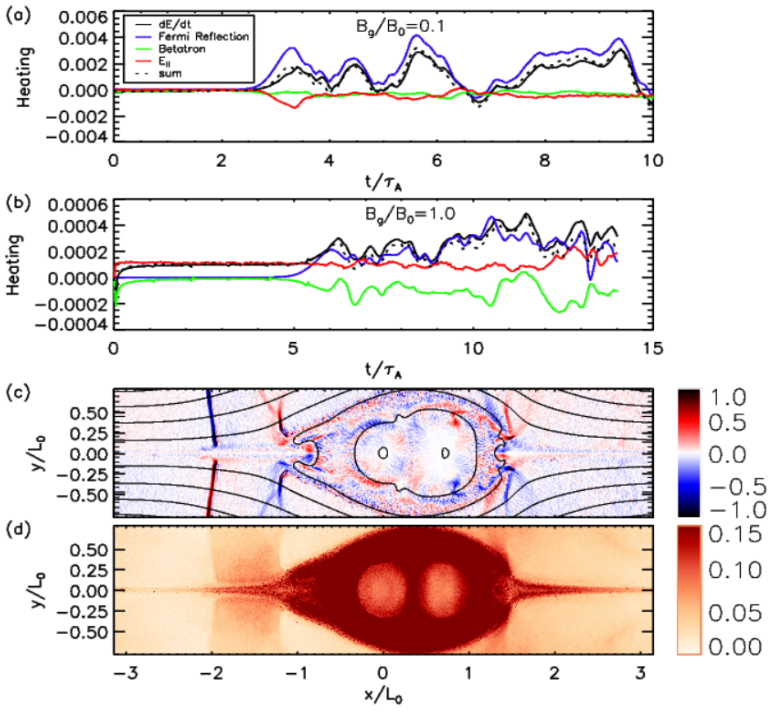

Figure 4.5: In panel (a): the heating of the particle electrons due to Fermi reflection (blue), the large scale parallel electric field (red), betatron acceleration (green), the sum of the previous three (dashed black), and the measured heating (black) versus time for B_g/B_0=1.0. In panel (b): the same but for $B_g/B_0 = 0.1$. In panel (c) and (d): the parallel electric field with field lines overplotted and $< W_{||} >$ respectively at late time for $B_g/B_0 = 0.025$ and initial electron temperature 0.02.

electron mass, T_M is the temperature (in energy units) of the Maxwellian, and W is the energy. Note that $\int F_{fit}(W)dW = N_\kappa + N_M$. Since the kappa function is a Maxwellian in the limit of low energy, we can further break up F_{fit} into a Maxwellian component, $F_M(W)$, a Maxwellian component from the kappa function, $F_{\kappa M}(W)$, and a nonthermal component from the kappa function that includes the power-law tail, $F_{\kappa NT}(W)$. To do this we follow the method laid out in [8]. We define a second Maxwellian temperature, $T_{\kappa M} \equiv (1/2)m_e\theta^2$, and set $F_{\kappa M}(T_M) = F_\kappa(T_M)$. This gives us an expression for the relative density and energy of the nonthermal electrons:

$$N_{NT} = N_\kappa - N_{\kappa M} = N_\kappa \left(1 - 2.718 \frac{\Gamma(\kappa+1)}{\Gamma(\kappa-1/2)} \kappa^{-3/2} \left(1 + \frac{1}{\kappa}\right)^{-(\kappa+1)}\right) \tag{4.5}$$

$$< W_{NT} >=< W_\kappa > - < W_{\kappa M} >= \frac{3}{2}T_\kappa - \frac{3}{2}T_{\kappa M} \tag{4.6}$$

where $T_\kappa = (1/2)m_e\theta^2[\kappa/(\kappa-3/2)]$. F_{fit} is overlaid in red on top of the particle data (in black) in the log-log plot in Fig. 4(a). In (b) F_{fit} is again overlaid in red over the particle data, but on a linear-linear scale zoomed in to low energies to more clearly see the thermal population. The dual Maxwellian-kappa function fits both the low and high energy particle data very well and can therefore be used to explore the relative numbers of hot thermal versus nonthermal electrons and the characteristic temperature of the hot thermals.

4.5.3 Analytic model of electron acceleration in a current sheet

We present a model for electron acceleration in a current layer with merging magnetic flux ropes that captures the essential results of the *kglobal* simulations,

including an expression for the power-law index of the nonthermal electrons and its dependence on the ambient guide field. The model includes both diffusion along the current layer as well as the convective loss of electrons injected into large, inactive flux ropes.

We first calculate electron energy gain during the merging of two flux ropes of radius r_i, azimuthal magnetic $B_{\theta i}$ and guide field B_g as shown in Fig. 3(c). Consistent with extensive PIC simulation results that the dominant electron heating is parallel to the local magnetic field [16, 27], we neglect plasma compression and associated betatron acceleration. Parallel heating results from the invariance of the parallel action $\oint v_{\parallel} dl$ as merging field lines contract from the figure-eight on the left of Fig. 3(c) to the circle on the right. Thus, the change in the energy during the merger of two flux ropes can be calculated by evaluating the geometry of the magnetic field before and after the merger. For an incompressible merger, the radius of the final flux rope is $r_f = \sqrt{2} r_i$ and the flux is preserved $r_f B_{\theta f} = r_i B_{\theta i}$ [30]. The effective field line length of the initial state is twice the length of a single flux rope, $s_i = 2\pi r_i B_i / B_{\theta i}$, where $B_i^2 = B_g^2 + B_{\theta i}^2$, since a reconnecting field line wraps around both flux ropes as can be seen by the recently reconnected field line in Fig. 3(c),. The final field line length is $s_f = 2\pi r_f B_f / B_{\theta f}$. Thus, invoking the invariance of the parallel action, the final electron parallel energy W_f is given by $W_i s_i^2 / s_f^2$. The energy change can be re-written as a rate equation for electron energy gain

$$\dot{W} = \frac{d}{dt} W = W \frac{g}{\tau_r}, \tag{4.7}$$

with $\tau_r \sim r_i / R c_{Ax}$, where $R \sim 0.1$ is the normalized rate of merger of the flux ropes

in the current layer, c_{Ax} the Alfvén speed based on the reconnecting magnetic field B_x of the current layer, and the factor $g = (1 + 2B_g^2/B_x^2)^{-1}$. The factor g describes the increase of the effective radius of curvature of the magnetic field in the presence of a guide field, which reduces the strength of Fermi reflection and associated energy gain during reconnection [16, 25, 28].

With the energy gain in Eqn. (4.7), we can write down an equation for the number density $F(x, W, t)$ of electrons per unit energy undergoing reconnection driven acceleration in a one-dimensional current layer and experiencing convective loss,

$$\frac{\partial}{\partial t}F + \frac{\partial}{\partial x}v_x(x)F + \frac{\partial}{\partial W}\dot{W}F - D\frac{\partial^2}{\partial x^2}F = \frac{1}{\tau_{up}}F_{up} \tag{4.8}$$

where $v_x(x)$ describes the convective loss of electrons as they are ejected at the Alfvén speed out of the current layer and we include a simple constant diffusion of electrons within the current layer. The electrons are injected into the layer with an initial distribution F_{up} which is taken as a low-temperature Maxwellian. Although the simulations carried out here are periodic and particles are therefore not lost, the large flux ropes that emerge at late time and no longer participate in the reconnection process act as sinks for energetic electrons [15, 87].

Further, as magnetic flux continues to be added to these flux ropes, electrons trapped in the islands become disconnected from the current layers. As in the classical problem of diffusive shock acceleration, the boundary condition on f at the injection point into the flux rope is zero slope.

The steady state solution of Eqn. (4.8) can be written as a sum of harmonics of $F \sim \sum_n F_n \cos(n\pi x/L)$, where we take the current layer to be centered at $x = 0$

and the injection in the large flux ropes to take place at $x = \pm L$ at the Alfvén speed c_{Ax}. However, the problem is simplified if the diffusion D is large so that the harmonics F_n with $n \neq 0$ are small. In this limit Eqn. (4.8) can simply be integrated over x to obtain an expression for F_0,

$$L\frac{\partial}{\partial W}\frac{Wg}{\tau_w}F_0 + c_{Ax}F_0 = \frac{L}{\tau_{up}}F_{up}. \tag{4.9}$$

This equation is readily inverted for F_0,

$$F_0 = \frac{1}{\tau_{up}}\frac{\tau_r}{gW}W^{-c_{Ax}\tau_r/gL}\int_0^W dW W^{c_{Ax}\tau_r/gL}F_{up}(W). \tag{4.10}$$

For low upstream temperature the energy integral can be extended to infinity and F_0 has the scaling

$$F_0 \propto \frac{1}{W}W^{-c_{Ax}\tau_r/gL} \sim W^{-(1+r_i/gRL)}. \tag{4.11}$$

The energetic spectrum takes the form of a power-law with a spectral index that depends on the rate of reconnection R, the relative size of the merging flux ropes that drive electron energy gain compared with the half-width of the current sheet L and the strength of the guide field.

Chapter 5: Conclusion

5.1 Summary

In this thesis we developed the new model *kglobal* for the purpose of studying nonthermal electron acceleration in macroscale magnetic reconnection. Unlike PIC codes we can simulate macroscale domains, and unlike MHD codes we can simulate particles that feedback onto the fluids so that the total energy of the system is conserved. This has never been done before. However, an important limitation of *kglobal* is, just like with MHD codes, the physics near the x-line, where the breaking of field lines takes place, is not correctly captured. This is because in the ion and electron diffusion regions, where reconnection takes place, the plasma species are no longer frozen into the magnetic field, and our assumptions are invalid. However, since the diffusion regions are not where most of the energy release of the magnetic field during reconnection takes place and in macrosystems the diffusion regions are negligible in size, particle energy gain should not depend on the details of the diffusion region. It has now been well established that the rate of energy release during reconnection in large systems is fast even in the MHD description. This is a consequence of the breakup of long current layers and multi-island reconnection in large systems [54–56, 93]

We have benchmarked the model by simulating Alfvén waves with electron pressure anisotropy, the growth of the firehose instability, and the growth of electron acoustic waves. Fermi reflection occurs when electrons reflect off of bent magnetic field lines travelling at the Alfvén speed. They then gain energy and induce a return current of cold electrons as they leave the reconnection exhaust, mediated by the electron acoustic wave. As more electrons are accelerated parallel to the magnetic field line via Fermi reflection, pressure anisotropy increases until reconnection is throttled as the plasma approaches the firehose stability boundary, eliminating the magnetic tension that drives reconnection. Thus, the model includes all of the essential physics that is needed to study nonthermal electron acceleration in magnetic reconnection.

We then studied the results of magnetic reconnection and found clear power-law tails that can extend for more than two decades in energy with a power-law index, δ', that decreases with the strength of the guide field. Reconnection in systems with guide fields approaching unity produce practically no nonthermal electrons. For weak guide fields the model is extremely efficient in producing nonthermal electrons. The nonthermals contain up to $\sim 80\%$ of the electron energy in our lowest guide field simulation. These results are generally consistent with flare observations and specifically the measurements of the September 10, 2017, flare.

An important characteristic of *kglobal* simulations is the clear power-law tails in the electron distribution. While power-law tails do develop in PIC simulations, they are more well developed in relativistic simulations [36, 78, 94–96] than in non-relativistic simulations where they extend only around a decade in energy [87]. The

reason why *kglobal* easily reproduced observed power-law tails is two-fold. Firstly, the electrons in *kglobal* are assumed to always be magnetized. This is a valid assumption since the Larmor radius of energetic electrons with energies between 1-10MeV and a typical solar flare magnetic field of 1-10G is 0.1-10m [97]. This is much smaller than the typical current sheet thickness in a solar flare which is likely 100-1000m [97] and is smaller than the magnetic islands that dominate magnetic energy release. Even in PIC simulations that are able to produce a power-law, energetic electrons become demagnetized and no longer gain energy [87]. This can be understood by first noting that the electrons corresponding to the upper edge of the power-law tail in [87] with an ion to electron mass ratio of 25, have a Larmor radius of $\sim 0.75d_i$, which is close to the initial current sheet width of $1d_i$, and are therefore demagnetized. Further, the turbulence spectrum shown in [87] shows strong turbulence at the scale of the energetic Larmor radius resulting in scattering and leading to isotropic energetic electrons. [30] showed that isotropic electrons no longer gain energy via Fermi reflection in magnetic reconnection. Thus, a power-law tail extending to higher energies is prevented once electrons become isotropic. This is the likely reason that PIC simulations are unable to produce the extensive power-laws seen in *klgobal*. However, if a PIC simulations could be run with realistic mass ratios and in much larger domains the Larmor radii of energetic electrons could be reduced below the characteristic island sizes and a more extended energetic tail would likely be produced. However, such simulations are not presently feasible.

A second problem with the PIC model is that the parallel electric field has been shown to suppress energy gain of nonthermal electrons [87]. In PIC simulations the

electric field in kinetic-scale boundary layers occupies a non negligible area near the x-line and along the separatrices. However, in an actual solar flare these boundary layers occupy a vanishingly small volume in comparison with the region of electron acceleration during island growth and merger. Thus, the artificially wide boundary layers and associated electric fields in the PIC model very likely also inhibit electron power-law formation.

Finally, there has been recent work suggesting that turbulence in MHD plasma follow a Kolmogorov-like cascade until they reach a critical length scale at which point current sheets undergoing magnetic reconnection are formed [98, 99]. The work presented in this thesis suggests that in collisionless, low β plasma with a small guide field, the energy will be released via Fermi reflection in a macroscale region downstream of the x-line. This is seemingly in contrast to the conventional picture of an energy cascade to small scales where dissipation takes place. However, as is noted in the scaling taken by [98], the guide field is likely large at these small scales. Thus, if reconnection is taking place at the small scale end of a turbulent cascade, we expect very few, if any, non-thermal electrons to be produced. A power-law distribution can likely only be formed via magnetic reconnection at larger macroscales, with only a small guide field where Fermi reflection dominates the energy conversion.

5.2 Future Work

Several questions remain to be answered that *kglobal* can help to answer. Further exploration of the slow shocks seen in our 2D reconnection simulations is needed

to explain thermal electron heating. Importantly, the heating mechanism is both independent of the guide field and the initial electron temperature. These shocks are seen in all of our simulations as well as those from MHD codes [43].

Further modifications to *kglobal* would also be helpful in continuing the exploration of particle acceleration. We intend to include pitch-angle scattering of energetic electrons since gyrosynchrotron observations require strong perpendicular heating that we do not see in our simulations [70]. A likely source of scattering is self-generated, off-angle whistler waves [100] which are not included in our model. However, we are developing a whistler-driven scattering operator that we hope to implement in *kglobal* to capture this important physics. Additionally, we intend to expand the model to include particle ions. This will allow us to study nonthermal ion acceleration, since ions account for a significant fraction of the energy released in solar flares [84, 101].

Bibliography

[1] J. Puerta and P. Martín. Plasma physics: Proceedings of the 1997 latin american workshop : Vii lawpp 97. *Springer*, page 57, 1999.

[2] M. Yamada. Progress in understanding magnetic reconnection in laboratory and space astrophysical plasmas. *Physics of Plasmas*, 14:058102, 2007.

[3] R. P. Lin and H.S. Hudson. 10-100 kev electron acceleration and emission from solar flares. *Solar Physics*, 17:412–435, 1971.

[4] A. G. Emslie, H. Kucharek, B. R. Dennis, N. Gopalswamy, G. D. Holman, G. H. Share, A. Vourlidas, T. G. Forbes, P. T. Gallagher, G. M. Mason, T. R. Metcalf, R. A. Mewaldt, R. J. Murphy, R. A. Schwartz, and T. H. Zurbuchen. Energy partition in two solar flare/cme events. *Journal of Geophysical Research*, 109:A10104, 2004.

[5] A. G. Emslie, B. R. Dennis, G. D. Holman, and H. S. Hudson. Refinements to flare energy estimates: A followup to 'energy partition in two solar flare/cme events' by a. g. emslie et al. *Journal of Geophysical Research*, 110:A11103, 2005.

[6] L. Sui and G. Holman. Evidence for the formation of a large-scale current sheet in a solar flare. *The Astrophysical Journal*, 596(2), 2003.

[7] S. Krucker, H. S. Hudson, L. Glesener, S. M. White, S. Masuda, J.-P. Wuelser, and R. P. Lin. Measurements of the coronal acceleration region of a solar flare. *The Astrophysical Journal*, 714:1108–1119, 2010.

[8] M. Oka, S. Ishikawa, P. Saint-Hilaire, S. Krucker, and R. P. Lin. Kappa distribution model for hard x-ray coronal sources of solar flares. *The Astrophysical Journal*, 764:6, 2013.

[9] M. Øieroset, R. P. Lin, T. D. Phan, D. E. Larson, and S. D. Bale. Evidence for electron acceleration up to 300 kev in the magnetic reconnection diffusion region of earth's magnetotail. *Physical Review Letters*, 89:195001, 2002.

[10] J. F. Drake, M. Swisdak, M. K. Schoeffler, B. N. Roger, and S. Kobayashi. Formation of secondary islands during magnetic reconnection. *Geophysical Research Letters*, 33:L13105, 2006.

[11] R. L Fermo, J. F. Drake, and M. Swisdak. Secondary magnetic islands generated by the kelvin helmholtz instability in a reconnecting current sheet. *Physical Review Letters*, 108:255005, 2012.

[12] R. Schreier, M. Swisdak, J. F. Drake, and P. A. Cassak. Three-dimensional simulations of the orientation and structure of reconnection x-lines. *Physics of Plasmas*, 17:110704, 2010.

[13] W. Daughton, V. Roytershteyn, H. Karimabadi, L. Yin, B. J. Albright, B. Bergen, and K. J. Bowers. Role of electron physics in the development of turbulent magnetic reconnection in collisionless plasmas. *Nature Physics*, 7:539–542, 2011.

[14] Y. Liu, W. Daughton, H. Karimabadi, H. Li, and V. Roytershteyn. Bifurcated structure of the electron diffusion region in three-dimensional magnetic reconnection. *Physical Review Letters*, 110:265004, 2013.

[15] J. T. Dahlin, J. F. Drake, and M. Swisdak. Electron acceleration in three-dimensional magnetic reconnection with a guide field. *Physics of Plasmas*, 22:100704, 2015.

[16] J. T. Dahlin, J. F. Drake, and M. Swisdak. The role of three-dimensional transport in driving enhanced electron acceleration during magnetic reconnection. *Physics of Plasmas*, 24:092110, 2017.

[17] C. T. Russell and R. C. Elphic. Initial isee magnetometer results: magnetopause observations. *Space Science Reviews*, 22:681–715, 1978.

[18] J. A. Slavin, R. P. Lepping, J. Gjerloev, D. H. Fairfield, M. Hesse, C. J. Owen, M. B. Moldwin, T. Nagai, A. Ieda, and T. Mukai. Geotail observations of magnetic flux ropes in the plasma sheet. *Journal of Geophysical Research*, 108:1015, 2003.

[19] L.-J. Chen, A. Bhattacharjee, P. A. Puhl-Quinn, H. Yang, N. Bessho, S. Imada, S. Mühlbachler, P. W. Daly, B. Lefebvre, Y. Khotyaintsev, A. Vaivads, A. Fazakerley, and E. Georgescu. Observation of energetic electrons within magnetic islands. *Nature Physics*, 4:19–23, 2008.

[20] D. E. McKenzi and H. S. Hudson. X-ray observations of motions and structure above a solar flare arcade. *The Astrophysical Journal Letters*, 519(1), 1999.

[21] Sl. Savage and D. McKenzi. Quantitative examination of a large sample of supra-arcade downflows in eruptive solar flares. *The Astrophysical Journal*, 730(2), 2011.

[22] E. P. Kontar, J. E. Perez, L. K. Harra, A. A. Kuznetsov, A. G. Emslie, N. L. S. Jeffrey, N. H. Bian, and B. R. Dennis. Turbulent kinetic energy in the energy balance of a solar flare. *PHYSICAL REVIEW LETTERS*, 118:155101, 2017.

[23] J. F. Drake, H. Arnold, M. Swisdak, and J. T. Dahlin. A computational model for exploring particle acceleration during reconnection in macroscale systems. *Physics of Plasmas*, 26:012901, 2019.

[24] B. Kliem. Particle orbits, trapping, and acceleration in a filamentary current sheet model. *Astrophysical Journal Supplement Series*, 90:719–728, 1994.

[25] J. F. Drake, M. Swisdak, H. Che, and M. Shay. Electron acceleration from contracting magnetic islands during reconnection. *Nature*, 443:553–556, 2006.

[26] J. F. Drake, M. Opher, M. Swisdak, and J. N. Chamoun. A magnetic reconnection mechanism for the generation of anomalous cosmic rays. *The Astrophysical Journal Letters*, 709:963, 2010.

[27] J. T. Dahlin, J. F. Drake, and M. Swisdak. The mechanisms of electron heating and acceleration during magnetic reconnection. *Physics of Plasmas*, 21:092304, 2014.

[28] J. T. Dahlin, J. F. Drake, and M. Swisdak. Parallel electric fields are inefficient drivers of energetic electrons in magnetic reconnection. *Physics of Plasmas*, 23:120704, 2016.

[29] C. Cattell, J. Dombeck, J. Wygant, J. F. Drake, M. Swisdak, M. L. Goldstein, W. Keith, A. Fazakerley, M. André, E. Lucek, and A Balogh. Cluster observations of electron holes in association with magnetotail reconnection and comparison to simulations. *Journal of Geophysical Research*, 110:A01211, 2005.

[30] Swisdak M. & Fermo R. Drake, J. F. The power-law spectra of energetic particles during multi-island magnetic reconnection. *The Astrophysical Journal Letters*, 763:L5, 2013.

[31] J. Egedal, W. Fox, N. Katz, M. Porkolab, M. Øieroset, R. P. Lin, W. Daughton, and J. F. Drake. Evidence and theory for trapped electrons in guide field magnetotail reconnection. *Journal of Geophysical Research*, 113:A12207, 2008.

[32] J. Egedal, W. Daughton, and A. Le. Large-scale electron acceleration by parallel electric fields during magnetic reconnection. *Nature Physics*, 8:321–324, 2012.

[33] J. Egedal, W. Daughton, A. Le, and A. L. Borg. Double layer electric fields aiding the production of energetic flat-top distributions and superthermal electrons within magnetic reconnection exhausts. *Physics of Plasmas*, 22:101208, 2015.

[34] C. C. Haggerty, M. A. Shay, J. F. Drake, T. D. Phan, and C. T. McHugh. The competition of electron and ion heating during magnetic reconnection. *Geophyscial Research Letters*, 42:9657–9665, 2015.

[35] D. Ball, L. Sironi, and F. Özel. Electron and proton acceleration in trans-relativistic magnetic reconnection: Dependence on plasma beta and magnetization. *The Astrophysical Journal*, 862:80, 2018.

[36] F. Guo, Y.-H. Liu, W. Daughton, and H. Li. Particle acceleration and plasma dynamics during magnetic reconnection in the magnetically dominated regime. *The Astrophysical Journal*, 806(2), 2015.

[37] G. Holman, L. Sui, R. Schwartz, and A. Emslie. Electron bremsstrahlung hard x-ray spectra, electron distributions, and energetics in the 2002 july 23 solar flare. *The Astrophysical Journal Letters*, 595(2), 2003.

[38] L. A. Fisk and G. Gloeckler. The common spectrum for accelerated ions in the quiet-time solar wind. *The Astrophysical Journal Letters*, 640(1), 2006.

[39] E. Stone, A. Cummings, F. McDonald, B. Heikkila, N. Lal, and W. Webber. An asymmetric solar wind termination shock. *Nature*, 454:71–74, 2008.

[40] R. B. Decker, S. M. Krimigis, E. C. Roelof, and M. E. Hill. Variations of low-energy ion distributions measured in the heliosheath. 1302:51, 2010.

[41] G. P. Zank, P. Hunana, P. Mostafavi, J. A. Le Roux, G. Li, G. M. Webb, O. Khabarova, A. Cummings, E. Stone, and R. Decker. Diffusive shock acceleration and reconnection acceleration processes. *The Astrophysical Journal*, 814(2), 2015.

[42] P. Montag, J. Egedal, E. Lichko, and B. Wetherton. Impact of compressibility and a guide field on fermi acceleration during magnetic island coalescence. *Physics of Plasmas*, 24(062906), 2017.

[43] X. Li, F. Guo, H. Li, and S. Li. Large-scale compression acceleration during magnetic reconnection in a low-β plasma. *The Astrophysical Journal*, 866(1), 2018.

[44] E. P. Kontar, N. Bian, A. Emslie, and N. Vilmer. Turbulent pitch-angle scattering and diffusive transport of hard x-ray-producing electrons in flaring coronal loops. *The Astrophysical Journal*, 780(2), 2014.

[45] M. Onofri, H. Isliker, and L. Vlahos. Stochastic acceleration in turbulent electric fields generated by 3d reconnection. *PHYSICAL REVIEW LETTERS*, 96:151102, 2006.

[46] J. Birn, M. F. Thomsen, and M. Hesse. Acceleration of oxygen ions in the dynamic magnetotail. *Annales Geophysicae*, 22:1305–1315, 2004.

[47] G. Kowal, E. de Gouveia Dal Pino, and A. Lazarian. Magnetohydrodynamic simulations of reconnection and particle acceleration: Three-dimensional effects. *The Astrophysical Journal*, 735(2), 2011.

[48] S. E. Guidoni, C. R. DeVore, J. T. Karpen, and B. J. Lynch. Magnetic-island contraction and particle acceleration in simulated eruptive solar flares. *The Astrophysical Journal*, 820:60, 2016.

[49] G. Tóth, X. Jia, S. Markidis, I. Peng, Y. Chen, L. Daldorff, V. Tenishev, D. Borovikov, J. Haiducek, T. Gombosi, A. Glocer, and J. Dorelli. Extended magnetohydrodynamics with embedded particle-in-cell simulation of ganymede's magnetosphere. *Journal of Geophysical Research*, 121:1273–1293, 2016.

[50] G. Lapenta, J. Brackbill, and P. Ricci. Kinetic approach to microscopic-macroscopic coupling in space and laboratory plasmas. *Physics of Plasmas*, 13:055904, 2006.

[51] M. Shay, J. F. Drake, B. N. Rogers, and R. E. Denton. The scaling of collisionless, magnetic reconnection for large systems. *Geophysical Research Letters*, 26:2163–2166, 1999.

[52] M. Shay, J. F. Drake, and M. Swisdak. Two-scale structure of the electron dissipation region during collisionless magnetic reconnection. *Physical Review Letters*, 99:155002, 2007.

[53] H. Karimabadi, W. Daughton, and J. Scudder. Multi-scale structure of the electron diffusion region. *Geophysical Research Letters*, 34:L13104, 2007.

[54] A. Bhattacharjee, Y.-M. Huang, H. Yang, and B. Rogers. Fast reconnection in high-lundquist-number plasmas due to the plasmoid instability. *Physics of Plasmas*, 16:112102, 2009.

[55] P. A. Cassak, M. A. Shay, and J. F. Drake. Scaling of sweet–parker reconnection with secondary islands. *Physics of PLasmas*, 16:120702, 2009.

[56] Y.-M. Huang and A. Bhattacharjee. Scaling laws of resistive magnetohydrodynamic reconnection in the high-lundquist-number, plasmoid-unstable regime. *Physics of Plasmas*, 17:062104, 2010.

[57] P. L. Pritchett and F. V. Coroniti. Three-dimensional collisionless magnetic reconnection in the presence of a guide field. *Journal of Geophysical Research*, 109:A01220, 2004.

[58] J. F. Drake, M. A. Shay, W. Thongthai, and M. Swisdak. Production of energetic electrons during magnetic reconnection. *Physical Review Letters*, 94:095001, 2005.

[59] Y. Lin and L. C. Lee. Structure of reconnection layers in the magnetosphere. *Space Science Reviews*, 65:59–179, 1993.

[60] C. Z. Cheng. A kinetic-magnetohydrodynamic model for low-frequency phenomena. *Journal of Geophysical Research*, 1991.

[61] W. Park, S. Parker, H. Biglari, M. Chance, L. Chen, C. Z. Cheng, T. S. Hahm, W. W. Lee, D. Kulsrud, and L. Monticello. Three-dimensional hybrid gyrokinetic-magnetohydrodynamics simulation. *Physics of PLasmas*, 4:2033, 1992.

[62] R. M. Kulsrud. Mhd description of plasma. *Basic Plasma Physics: Selected Chapters, Handbook of Plasma Physics*, 1:115–144, 1983.

[63] X.-N. Bai, D. Caprioli, L. Sironi, and A. Spitkovsky. Magnetohydrodynamic-particle-in-cell method for coupling cosmic rays with a thermal plasma: Application to non-relativistic shocks. *The Astrophysical Journal*, 809(1), 2015.

[64] C. Tronci, E. Tassi, E. Camporeale, and P. Morrison. Hybrid vlasov-mhd models: Hamiltonian vs. non-hamiltonian. *Plasma Physics and Controlled Fusion*, 56(9), 2014.

[65] R. P. Lin, S. Krucker, G. J. Hurford, D. M. Smith, H. S. Hudson, and G. D. Holman. *RHESSI* observations of particle acceleration and energy release in an intense solar gamma-ray line flare. *The Astrophysical Journal*, 595:L69–L76, 2003.

[66] E. N. Parker. The passage of energetic charged particles through interplanetary space. *Planetary and Space Science*, 13:9–49, 1965.

[67] X. Li, F. Guo, H. Li, and J. Birn. The roles of fluid compression and shear in electron energization during magnetic reconnection. *The Astrophysical Journal*, 855(2), 2018.

[68] T. Northrop. Adiabatic charged-particle motion. *Reviews of Geophysics*, 1:283, 1963.

[69] H. Nakajima, M. Nishio, S. Enome, K. Shibasaki, T. Takano, Y. Hanaoka, C. Torii, H. Sekiguchi, T. Bushimata, S. Kawashima, N. Shinohara, Y. Irimajiri, H. Koshiishi, T. Kosugi, Y. Shiomi, M. Sawa, and K. Kai. The nobeyama radioheliograph. *Proceedings of the IEEE*, 82(5):705–713, 1994.

[70] D. E. Gary, B. Chen, B. R. Dennis, G. D. Fleishman, G. J. Hurford, and S. Krucker. Microwave and hard x-ray observations of the 2017 september 10 solar limb flare. *The Astrophysical Journal*, 863:83, 2018.

[71] E. N. Parker. Dynamics of the interplanetary gas and magnetic fields. *Astrophysical Journal*, 128:664, 1958.

[72] M. A. Shay, J. F. Drake, M. Swisdak, W. Dorland, and B. N. Rogers. Inherently three dimensional magnetic reconnection: A mechanism for bursty bulk flows? *Geophysical Research Letters*, 30(6):1345, 2003.

[73] A. Zeiler, D. Biskamp, J. F. Drake, B. N. Rogers, M. A. Shay, and M. Scholer. Three-dimensional particle simulations of collisionless magnetic reconnection. *Journal of Geophysical Research*, 107:1230, 2002.

[74] H. Arnold, J. Drake, M. Swisdak, and J. Dahlin. Large-scale parallel electric fields and return currents in a global simulation model. *Physics of Plasmas*, 26:102903, 2019.

[75] Y. Liu, M. Hess, F. Guo, W. Daughton, H. Li, P. Cassak, and M. Shay. Why does steady-state magnetic reconnection have a maximum local rate of order 0.1? *Physical Review Letters*, 118:085101, 2017.

[76] D. A. Uzdensky, N. F. Loureiro, and A. A. Schekochihin. Fast magnetic reconnection in the plasmoid-dominated regime. *Physical Review Letters*, 105:235002, 2010.

[77] S. Gary and R. Tokar. The electron-acoustic mode. *Physics of Fluids*, 28:2439, 1985.

[78] F. Guo, H. Li, W. Daughton, and Y. Liu. Formation of hard power laws in the energetic particle spectra resulting from relativistic magnetic reconnection. *Physical Review Letters*, 113:155005, 2014.

[79] H. P. Warren, D. H. Brooks, I. Ugarte-Urra, J. W. Reep, N. A. Crump, and G. A. Doschek. Spectroscopic observations of current sheet formation and evolution. *The Astrophysical Journal*, 854:2, 2018.

[80] B. Chen, C. Shen, D. Gary, K. Reeves, G. Fleishman, S. Yu, F. Guo, S. Krucker, J. Lin, G. Nita, and X. Kong. Measurement of magnetic field and relativistic electrons along a solar flare current sheet. *Nature Astronomy*, 2020.

[81] Fleishman, Gary G. D., D. E., B. Chen, N. Kuroda, S. Yu, and G. M. Nita. Decay of the coronal magnetic field can release sufficient energy to power a solar flare. *Science*, 367:6475, 2020.

[82] H. Arnold, J. F. Drake, M. Swisdak, F. Guo, J. T. Dahlin, B. Chen, G. Fleishman, L. Glesener, E. Kontar, T. Phan, and C. Shen. Electron acceleration during macroscale non-relativistic magnetic reconnection. *arXiv.org*, 2020.

[83] P. K. Kaw, E. J. Valeo, and P. H. Rutherford. Tearing modes in a plasma with magnetic braiding. *Physical Review Letters*, 43:1398, 1979.

[84] A. G. Emslie, B. R. Dennis, A. Y. Shih, P. C. Chamberline, R. A. Mewaldt, C. S. Moore, G. H. Share, A. Vourlidas, and B. T. Welsch. Global energetics of thirty-eight large solar eruptive events. *The Astrophysical Journal*, 759:71, 2012.

[85] M. Aschwanden, G. Holman, A. O'Flannagain, A. Caspi, J. McTiernan, and E. Kontar. Global energetics of solar flares. iii. nonthermal energies. *The Astrophysical Journal*, 832:27, 2016.

[86] A. Warmuth and G. Mann. Constraints on energy release in solar flares from rhessi and goes x-ray observations. *Astronomy and Astrophysics*, 588:A115, 2016.

[87] X. Li, F. Guo, H. Li, A. Stanier, and P. Kilian. Formation of power-law electron energy spectra in three-dimensional low-β magnetic reconnection. *The Astrophysical Journal*, 884:118, 2019.

[88] J. Lin and T. G. Forbes. Effects of reconnection on the coronal mass ejection process. *Journal of Geophysical Research*, 105:2375–2392, 2000.

[89] X. Cheng, Y. Li, M. Wan, L.and Ding, P. Chen, J. Zhang, and J. Liu. Observations of turbulent magnetic reconnection within a solar current sheet. *The Astrophysical Journal*, 866(1), 2018.

[90] C. C. Haggerty, M. A. Shay, A. Chasapis, T. D. Phan, J. F. Drake, K. Malakit, P. Cassak, and R. Kieokaew. The reduction of magnetic reconnection outflow jets to sub-alfvénic speeds. *Phyiscs of Plasmas*, 25:102120, 2018.

[91] L. Glesener, S. Krucker, J. Duncan, I. Hannah, B. Grefenstette, Chen B., D. Smith, S. White, and H. Hudson. Accelerated electrons observed down to ¡7 kev in a nustar solar microflare. *The Astrophysical Journal*, 891(2), 2018.

[92] Q. Zhang, J. F. Drake, and M. Swisdak. Instabilities and turbulence in low-β guide field reconnection exhausts with kinetic riemann simulations. *Physics of Plasmas*, 26:102115, 2019.

[93] W. Daughton, V. Roytershteyn, B. J. Albright, H. Karimabadi, L. Yin, and K. Bowers. Transition from collisional to kinetic regimes in large-scale reconnection layers. *Physical Review Letters*, 103:065004, 2009.

[94] F. Guo, X. Li, W. Daughton, P. Kilian, H. Li, Y. Liu, W. Yan, and D. Ma. Determining the dominant acceleration mechanism during relativistic magnetic reconnection in large-scale systems. *The Astrophysical Journal Letters*, 879:L23, 2019.

[95] L. Sironi and A. Spitkovsky. Relativistic reconnection: An efficient source of non-thermal particles. *The Astrophysical Journal Letters*, 783(1), 2014.

[96] G. R. Werner, D. A. Uzdensky, B. Cerutti, K. Nalewajko, and M. C. Begelman. The extent of power-law energy spectra in collisionless relativistic magnetic reconnection in pair plasmas. *The Astrophysical Journal Letters*, 816(1), 2016.

[97] M. Gordovskyy, P. Browning, and R. Pinto. Combining mhd and kinetic modelling of solar flares. *Advances in Space Research*, 63:1453–1465, 2019.

[98] S. Boldyrev and N. Loureiro. Magnetohydrodynamic turbulence mediated by reconnection. *The Astrophysical Journal*, 844, 2017.

[99] N. Loureiro and S. Boldyrev. Nonlinear reconnection in magnetized turbulence. *The Astrophysical Journal*, 890, 2020.

[100] G. T. Roberg-Clark, O. Agapitov, J. F. Drake, and M. Swisdak. Scattering of energetic electrons by heat-flux-driven whistlers in flares. *The Astrophysical Journal*, 887(2), 2019.

[101] M. Aschwanden, A. Caspi, C. Cohen, G. Holman, J. Jing, M. Kretzschmar, E. Kontar, J. McTiernan, R. Mewaldt, A. O'Flannagain, I. Richardson, D. Ryan, H. Warren, and Y. Xu. Global energetics of solar flares and cmes: V. energy closure. *The Astrophysical Journal*, 836(1), 2017.